NONLINEAR SPECTROSCOPY FOR CHARACTERIZING CELLS, PROTEINS, AND THE ORIGINS OF THE PHOTOBIOMODULATION EFFECT

A Dissertation

by

SEAN PATRICK O'CONNOR

Submitted to the Graduate and Professional School of
Texas A&M University
in partial fulfillment of the requirements for the degree of

DOCTOR OF PHILOSOPHY

Chair of Committee,	Marlan O. Scully
Co-Chair of Committee,	Vladislav V. Yakovlev
Committee Members,	Alexei V. Sokolov
	Aleksei M. Zheltikov
Head of Department,	Grigory V. Rogachev

May 2022

Major Subject: Applied Physics

ABSTRACT

The introduction of the laser in the 1960s brough forth the discovery of many nonlinear phenomena and marked the beginning of the field of nonlinear optics. Nonlinear spectroscopy offers many additional features over conventional linear spectroscopy which can be useful towards biomedical applications. In this work, we employ nonlinear spectroscopy and phenomena towards solving problems in biomedical fields.

In the first study, the visible light generation following filamentation is studied to address knowledge gaps within the American National Standard for the Safe Use of Lasers (ANSI Z136.1-2014). The ANSI standards provide maximum permissible exposure (MPE) values for skin and retinal tissue; however, nonlinear optical effects that cause visible light generation are currently not addressed. In this study, we measure the visible light following filamentation of ultrafast near- to mid- infrared (IR) light. Near-IR light, which normally attenuates before reaching the retina in the eye, was found to generate sufficient visible light following filamentation to exceed the MPE values set by ANSI.

In the next two studies, ultrafast transient absorption spectroscopy is used to study the mechanisms underlying the photobiomodulation (PBM) effect. PBM is the use of low irradiance light in the red to near-IR range to stimulate beneficial effects in tissues and cells. However, the electronic or molecular mechanisms which initiate that effect are not well understood. In our first study, we introduce a novel methodology which couples a continuous wave (CW) laser with ultrafast transient absorption spectroscopy (TAS), coined as CW-TAS, and test the proof-of-principle with the mitochondrial protein,

cytochrome c (Cyt c). The TAS data for Cyt c remained intact and unperturbed with the addition of the CW light compared to standard TAS. This indicated that CW-TAS can be used on the more complex mitochondrial proteins suspected to be involved in PBM, and it provided further evidence that Cyt c was not an initiator of the PBM effect. In our second study, we apply the CW-TAS technique to the more complex mitochondrial protein, Complex III (C-III), from a mammalian source. This study provided the first TAS characterization for C-III from specifically a mammalian source. In addition, the photodissociation and recombination of the axial ligand that was tested with TAS was found to not exhibit changes when measured with CW-TAS. Therefore, we conclude that this electronic process of C-III is eliminated from being a potential initiator of the PBM effect.

In the final study, beam shaping techniques were applied to improve the spectral resolution of impulsive stimulated Brillouin scattering (ISBS) spectroscopy towards cellular studies. Brillouin spectroscopy, which studies the elastic properties of materials, has been demonstrated to be useful for biomedical imaging and sensing. In particular, ISBS microscopy has recently been introduced towards biomedical applications; however, improvements to the spectral resolution have not been currently addressed. In this study, we expand the initial pump beam diameter with a 4f configuration and employ the use of a cylindrical lens to focus it into the system. The ISBS linewidth in the Fourier domain was found to be dependent on the pump beam’s spatial geometry. By increasing the spectral resolution, close elastic signals can be resolved which is important in biological and cellular studies where samples contain a high water content.

DEDICATION

To my family, whose love and support made this all possible.

ACKNOWLEDGEMENTS

To begin, I would like to first thank my advisors, Dr. Marlan Scully and Dr. Vladislav Yakovlev, for all of their guidance and support in my graduate studies. Dr. Scully, thank you so much for the opportunity to do research with the Institute for Quantum Science and Engineering all those years ago. Accepting that offer changed my life in ways I could not imagine, and I cannot thank you enough. Dr. Yakovlev, thank you so much for your patience with me in my learning process, thank you for your guidance, and thank you for all of the wonderful opportunities that you have provided to me. I would also like to thank the other members of my committee, Dr. Alexei Sokolov and Dr. Aleksei Zheltikov. Dr. Sokolov, thank you for all of your guidance, thank you for your kindness, and thank you for your lessons in nonlinear and ultrafast optics which helped my understanding in my research. Dr. Zheltikov, thank you for your kindness and your lessons in quantum mechanics which have helped me to this day. My studies were made entirely possible by the support and guidance of my committee, and I am incredibly grateful.

I would also like to thank my friends in my lab group for making the experience all the more enjoyable: Christopher Marble, Dominik Doktor, Kassie Marble, Mark Keppler, Joseph Harrington, Arthur Alvarez, Jace Willis, Joshua Lalonde, Vsevolod Cheburkanov, Eddie Gil, Dr. Anton Shutov, Dr. Dawson Nodurft, Dr. Zachary Coker, and Dr. Georgi Petrov. I would like to particularly thank: Chris, thank you for being a great friend all of these years. I really enjoyed our conversations together, and it was always a highlight in my day. I look forward to seeing the great things you will do! Dom, thank you for being a great friend and a great lab partner. I enjoyed our time together having fun discussions, getting good lab results, and going for coffee breaks! I look forward to seeing you do well as a PhD student! Kassie, thank you for being a cool person and a good friend. I look forward to seeing you do well! Joey, thank you for being a good friend, and keep hanging in there! Mark and Josh, thank you for all of the good times during our research summers in San Antonio! Dawson, thank you for your friendship and all of your guidance, I appreciate your mentorship immensely.

I also want to thank everyone in the department at Texas A&M University! I want to thank my friends at Texas A&M University: Stefania Dede, Christapher Vincent, Jeffrey Breitschopf, Mrunal Kamble, Aysan Bahari, Mariia Shutova, Debsuvra Mukhopadhyay, Navid Rajil, Shahriar Esmaeili, Sahar Delfan, Dr. Arash Azizi, Dr. Alma Fernández-González, Dr. Alexandra Zhdanova, Dr. Zhenhuan Yi, and so many more! I also want to thank the support staff for all of their help along the way: RaéChel Superville, Sherree Kessler, Veronica Rodriguez, Frances Ellison, Geoffrey Franceschi, Garrick Garza, Leo Garza, Robert Gunn, Brendan Martin, Mary Louise Sims, Michelle Sylvester, Barbara Siems, and Heather Walker. Also, I want to thank Yasa Rathnayaka and Kim Chapin for all of their wonderful help in IQSE along the way. I want to thank my professors for all of their lessons in lecture. I particularly want to thank: Dr. M. Suhail Zubairy for his wonderful class in quantum optics which really helped to enrich my understanding of the field. Dr. Tatiana Erukhimova, thank you for having me as a DEEP mentor and for making physics inspiring and fun!

In addition, I would like to thank my colleagues and friends at the Air Force Research Laboratory at Ft. Sam Houston: Dr. Michael Denton, Mr. J. Michael Rickman, Dr. Samantha Powell, Dr. Nathaniel Pope, Mr. Gary Noojin, Dr. Andrew Wharmby, Dr. Morgan Schmidt, Dr. Robert Thomas, and Dr. Benjamin Rockwell. I would like to particularly thank: Dr. Denton, thank you for all of your guidance in the realm of biology, and thank you for the opportunity to work with you on the photobiomodulation research. This opportunity was incredible, and I've learned so much. I cannot thank you enough.

And finally, I cannot possibly thank my family enough for all of their love and support in my life which helped to make my dreams possible. To my Mom, thank you for always reassuring me when I was feeling down, thank you for the sacrifices you made to give my brother and I a good education in Texas, and thank you for always helping me stay positive and motivated! To my Dad, thank you so much for inspiring me to reach for the stars, thank you for everything that you have done for my brother and I, and thank you for teaching me that with the right attitude, nothing is impossible! To my brother, Brandon, thank you for being the best brother I could ever have, and thank you for helping to keep my head on straight during this adventure. I always enjoyed our time growing up playing games, watching anime, and working out together. I look forward to seeing you be a great father for little Patrick! To my grandmother, Oma, thank you so much for always cheering me on and supporting me along the way. To all of my family, from the bottom of my heart, thank you so much, for everything!

CONTRIBUTORS AND FUNDING SOURCES

Contributors

This work was supervised by a dissertation committee consisting of Professor Marlan O. Scully [co-advisor] of the Department of Physics and Astronomy, Professor Vladislav V. Yakovlev [co-advisor] of the Department of Biomedical Engineering, and Professors Alexei V. Sokolov and Aleksei M. Zheltikov of the Department of Physics and Astronomy.

The data collected and analyzed for Chapter 2 was done in collaboration with Christopher Marble and Dr. Dawson Nodurft of the Department of Physics and Astronomy. The sample preparation and data collection for Chapter 3 and 4 was done in collaboration with Dr. Samantha Powell of the Air Force Research Laboratory. The experimental setup and data collection for Chapter 5 was done in collaboration with Dominik Doktor of the Department of Physics and Astronomy. All other work conducted for the dissertation was completed by the student independently.

Funding Sources

Graduate study was supported by the Herman F. Heep and Minnie Belle Heep Texas A&M University Endowed Fund held/administered by the Texas A&M Foundation, and by the Robert A. Welch Foundation under Grant No. A-1261.

This work was also made possible in part by the National Science Foundation (NSF) (DBI-1532188, DBI-1455671, ECCS-1509268, PHY-2013771, CMMI-1826078), the Air Force Office of Scientific Research (AFOSR) (FA9550-15-1-0517, FA9550-18-

1-0141, FA9550-20-1-0366, 19RHCOR067), the Army Research Laboratory (ARL) (W911NF-17-2-0144), DOD Army Medical Research (W81XWH2010777), the Office of Naval Research (ONR) (N00014-16-1-3054, N00014-20-1-2184, N00014-16-1-2578), the U.S. Department of Defense (FA9550-15-1-0517, FA9550-18-1-0141, N00014-16-1-2578), the National Institutes of Health (NIH) (1R01GM127696-01, 1R21GM142107), and the Cancer Prevention Research Institute of Texas (RP160834, RP180588).

TABLE OF CONTENTS

LIST OF FIGURES

Page

LIST OF TABLES

Page

1. INTRODUCTION

1.1. Background for Nonlinear Optics

Spectroscopy is the study of the interactions between light and matter where the resulting signal is measured as a function of the light's wavelength or frequency. By measuring and analyzing the light that follows from the interaction with a material sample, different properties about that sample can be obtained, such as optical properties or structural properties. Prior to the 1960s, the most common type of spectroscopies were linear spectroscopies where the electrons in a sample interact with only one light particle (one "photon") in the interaction. However, this changed with the construction of the first working laser by Theodore H. Maiman in 1960 at the Hughes Research Laboratories [1], based on the theoretical framework by Charles H. Townes and Arthur L. Schawlow published in 1958 [2].

Shortly thereafter, the field of "nonlinear optics" was born with the discovery of second-harmonic generation (SHG) by Peter A. Franken *et al.* in 1961 [3]. In their experiment, a ruby laser with a wavelength of 694 nm was focused onto a sample of quartz and the output was measured with a spectrometer. In the spectra, there was a signal at measured at 694 nm due to the unperturbed source beam and there was also a signal measured at 347 nm, at the second harmonic. The 347 nm beam was at half the wavelength of the source beam, and thus, twice the frequency and energy. This observation of harmonic generation in optical waves was made possible by the application of the laser due to its high intensity output. This led to the birth of the field of nonlinear optics.

Nonlinear optics is the study of light-matter interactions in which the material's response to the applied optical field depends nonlinearly on the strength of the optical field [4]. For example, SHG is a nonlinear optical phenomenon that occurs as a result of the atomic response that scales quadratically with respect to the applied optical field. As a consequence of this, the intensity of the second harmonic light generated in SHG tends to increase proportionally to the square of the intensity of the applied source light. SHG is one of many different nonlinear optical effects that have been discovered since the advent of laser technology. In the following section, we will provide a brief introduction into nonlinear optical theory which will motivate each of the nonlinear spectroscopies used in the scope of this work.

1.2. Nonlinear Optical Theory

1.2.1. Nonlinear polarization

The following treatment of nonlinear optical theory will follow from Robert Boyd's "Nonlinear Optics" [4]. In conventional optics and classical electromagnetic theory, the polarization $P(t)$ of a material is linearly dependent on the applied electric field $E(t)$ described by Equation 1.1.

$$\tilde{P}(t) = \epsilon_0 \chi^{(1)} \tilde{E}(t) \tag{1.1}$$

Here, ϵ_0 is the permittivity of free space, $\chi^{(1)}$ is the linear susceptibility, and the tilde (~) denotes that the quantity oscillates rapidly in time. At high electric field strengths, such as with the application of a laser as the applied field, the polarization no longer maintains a linear dependence on the applied field. In nonlinear optics, the polarization is more appropriately expressed as a power series in the electric field strength, described by Equation 1.2.

$$\tilde{P}(t) = \epsilon_0\left(\chi^{(1)}\tilde{E}(t) + \chi^{(2)}\tilde{E}^2(t) + \chi^{(3)}\tilde{E}^3(t) + \cdots\right) \tag{1.2}$$

$$\tilde{P}(t) = \tilde{P}^{(1)}(t) + \tilde{P}^{(2)}(t) + \tilde{P}^{(3)}(t) + \cdots \tag{1.3}$$

Here, $\chi^{(2)}$ and $\chi^{(3)}$ are the second-order and third-order nonlinear susceptibilities, respectively. In addition, $\tilde{P}^{(2)}(t) = \epsilon_0\chi^{(2)}\tilde{E}^2(t)$ is the second-order nonlinear polarization and $\tilde{P}^{(3)}(t) = \epsilon_0\chi^{(3)}\tilde{E}^3(t)$ is the third-order nonlinear polarization.

We briefly note here that the expression for the nonlinear polarization as written in Equation 1.2 is written in the scalar form for simplicity. In a more general form, the polarization and electric field are vector quantities, and the susceptibilities $\chi^{(n)}$ are rank $(n + 1)$ tensors (for example, $\chi^{(1)}$ is a rank 2 tensor). In addition, it is written with the assumption that the medium is lossless and without dispersion. More general expressions that account for loss and dispersion can be found in detail in Section 1.3 of Boyd's "Nonlinear Optics" [4].

1.2.2. Optical Kerr effect

When intense light is incident upon a medium, the light can induce a variation in the index of refraction which is directly proportional to the intensity of that light. This results in an intensity dependent index of refraction (n), also known as the optical Kerr effect, which is described in Equation 1.4.

$$n = n_0 + n_2 I \tag{1.4}$$

Here, n_0 is the linear refractive index that low intensity light would usually experience, n_2 is the nonlinear refractive index, and I is the intensity of the incident light. The optical

Kerr effect comes from the third-order nonlinear susceptibility $\chi^{(3)}$ of the material and is related to the nonlinear refractive index n_2 by the expression given in Equation 1.5.

$$n_2 = \frac{3}{4n_0^2\epsilon_0 c}\chi^{(3)} \tag{1.5}$$

Here, ϵ_0 is the permittivity of free space and c is the vacuum speed of light. To provide references for some typically observed values, some experimentally measured values for n_2 (and the computed $\chi^{(3)}$ values) are tabulated in Table 1.1 for different mediums, such as air, water, and commonplace optical materials. The intensity dependent index of refraction leads to many interesting physical consequences, because the optically modified medium can then modify the incident optical field. This results in many interesting effects such as (but not limited to): self-focusing [5], self-phase modulation [6,7], self-steepening [8], and filamentation [9,10].

Table 1.1 Experimentally measured n_2 values for different optical media, and the associated $\chi^{(3)}$ value computed using Equation 1.5. The Sellmeier equation was used to compute the adjustment to the linear refractive index n_0 for each medium based on the source wavelength.

Medium	Wavelength (nm)	n_0	n_2 (cm^2/W)	$\chi^{(3)}$ (m^2/V^2)	Reference
Air	800	1.0003	3.0×10^{-19}	1.1×10^{-25}	[11]
Water	1064	1.326	4.1×10^{-16}	2.6×10^{-22}	[12]
BK7 glass	1064	1.4496	2.1×10^{-16}	1.6×10^{-22}	[13]
Fused silica	1030	1.45	2.2×10^{-16}	1.6×10^{-22}	[14]
ZnSe	1064	2.472	2.9×10^{-14}	6.3×10^{-20}	[15]

The self-focusing of light refers to when intense light modifies the optical properties of the medium such that the medium then causes the light to focus while propagating in the medium. The high intensity of the light modifies the effective index of refraction due to the optical Kerr effect (see Equation 1.4) proportional to the light intensity. Since the center of the beam profile is more intense than the peripheral for lasers, the effective index of refraction of the material is modified more strongly where the center of the beam propagates than the peripheral of the beam. As a result, a gradient of effective refractive indices forms in the medium due to the beam's intensity distribution. For nonlinear index $n_2 > 0$ (as is the case for most materials), the optically modified material behaves like a positive lens, causing the beam to focus while propagating in the medium.

1.3. Filamentation

The following section on filamentation follows from the comprehensive article on the subject matter written by Arnaud Couairon and André Mysyrowicz [10] as well as from chapter 7 in Robert Boyd's "Nonlinear Optics" [4]. Filamentation is a nonlinear optical phenomenon where intense laser pulses undergo self-focusing and overcome pulse diffraction to propagate distances much larger than the diffraction length while maintaining a narrow beam diameter. This occurs when the laser pulse has a power that is greater than what is known as the critical power threshold P_{cr}, defined in Equation 1.6.

$$P_{cr} = \frac{C\lambda^2}{8\pi n_0 n_2} \tag{1.6}$$

Here, λ is the wavelength of the initial pulse, n_0 is the linear refractive index of the medium, n_2 is the nonlinear index of the medium, and C is a numerical factor based on the shape of the beam profile. In the general case, the numerical factor is between the values of $3.72 < C < 6.4$ [16]. Specific examples include $C \approx 3.72$ for a Townes beam and $C \approx 3.77$ for a Gaussian beam [10].

Filamentation occurs when the incident laser power is greater than the critical power ($P_{in} > P_{cr}$). Figure 1.1 displays a schematic representation of the filamentation process. The critical power P_{cr} is defined as the power that the incident laser pulse must have for the self-focusing of the pulse to balance exactly against the natural divergence of the laser due to diffraction. Therefore, the self-focusing overcomes diffraction when $P_{in} > P_{cr}$, and this focusing causes the beam to collapse in diameter and thus increase in intensity. When the intensity is sufficiently high, multiphoton ionization of the medium begins to occur which partially attenuates the laser pulse’s core intensity and results in the generation of a plasma in the medium. This plasma causes a local reduction in the index of refraction and acts to defocus the beam [17]. Once defocused, the pulse may still have a power above the critical power threshold and enter another focusing-defocusing cycle. This is the process of filamentation, and the part of the pulse propagation where the column of weakly ionized plasma is generated is referred to as the filament.

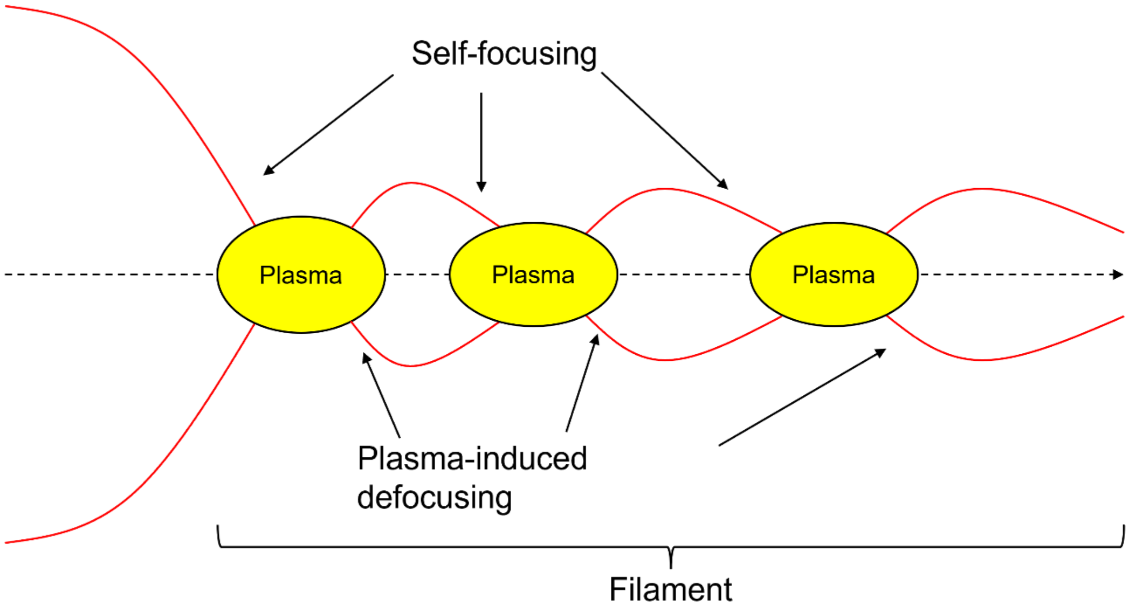

Figure 1.1 Schematic representation of filamentation. The solid red curves indicate the intense core of the laser beam, and the black dashed arrow indicates the axis of pulse propagation. Adapted from Couairon *et al.*, "Femtosecond filamentation in transparent media" [10].

1.4. Transient Absorption Spectroscopy

Transient absorption spectroscopy (TAS) is a pump-probe spectroscopic technique which probes and characterizes the excited dynamics of molecules and chemical processes with a high temporal resolution. Typically for linear spectroscopic techniques, the time-resolution of a measurement can be limited by the speed of the detector, which can be on the order of nanoseconds. However, for pump-probe spectroscopies such as TAS, the time-resolution is only limited by the time-duration of the pump and probe pulses. With the use of a femtosecond laser source for the pump and probe pulses, ultrafast TAS can achieve a sub-picosecond timescale which allows for the biological and chemical photo-processes to be resolved [18].

A schematic of the principle of TAS is displayed in Figure 1.2. In TAS measurements, a fraction of the sample is first excited with a pump pulse which is then followed by a white light (supercontinuum) probe pulse with a time delay Δt between the pulses. After passing through the sample, the remaining pump pulse is blocked, and the white light probe is measured with a spectrometer. Following the pump-probe measurement, a measurement with only the probe pulse without the pump pulse is taken for the ground state measurement. In TAS, the excited absorbance measurement and ground-state absorbance measurement are both used to compute a difference absorbance $\Delta A(\lambda)$ at that time delay. This process is repeated for at different time delays Δt to build the difference absorbance $\Delta A(\lambda, \Delta t)$ data set which is surface data depending on the two parameters: wavelength λ and time delay Δt.

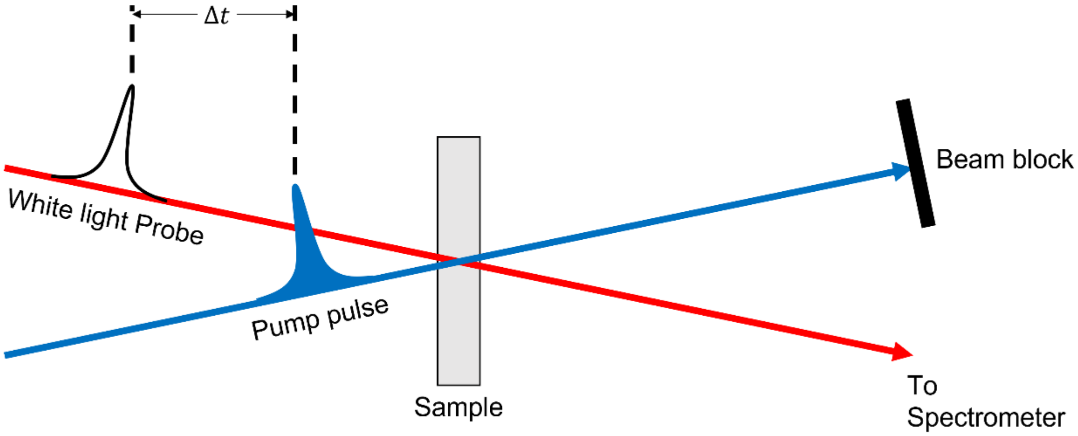

Figure 1.2 Schematic representation of transient absorption spectroscopy. Here, Δt is the time delay between the pump and probe pulses.

The difference absorbance spectrum $\Delta A(\lambda)$ can be presented as a difference of the pumped (excited) sample absorbance and unpumped (ground-state) sample absorbance as shown in Equation 1.7.

$$\Delta A(\lambda, \Delta t) = A_{pumped}(\lambda, \Delta t) - A_{unpumped}(\lambda) \tag{1.7}$$

The absorbance A is related to the transmittance T of light in a sample by the relation in Equation 1.8, and the transmittance can be expressed in terms of the intensity of light before (I_0) and after (I) passing through the sample.

$$A = -\log_{10}(T) \tag{1.8}$$

$$T = \frac{I}{I_0} \tag{1.9}$$

In TAS experiments, the measurements being are being made by the spectrometer are of the final intensity (I) of the pumped sample ($I = I_{pumped}(\lambda, \Delta t)$ and of the unpumped sample ($I = I_{unpumped}$). With careful tuning of the probe pulses for spectral consistency from pulse-to-pulse and taking enough averaging, the initial probe intensity I_0 on the sample can be considered to be equivalent between the pumped and unpumped samples. Therefore, Equations 1.7-1.9 can be used to derive the expression in Equation 1.10 for the difference absorbance spectrum $\Delta A(\lambda)$.

$$\Delta A(\lambda) = -\log_{10}\left(\frac{I_{pumped}(\lambda, \Delta t)}{I_{unpumped}(\lambda)}\right) \tag{1.10}$$

This is how the $\Delta A(\lambda)$ spectrum for each time delay Δt is calculated by the computer software from the measurements taken in TAS experiments.

1.5. Impulsive Stimulated Brillouin Spectroscopy

This section follows in part from the discussion in the book section “Transient Grating Experiments in Glass-Former Liquids” by Renato Torre and his coworkers [19]. Impulsive stimulated Brillouin scattering (ISBS) is a form of the stimulated Brillouin scattering (SBS) phenomenon that takes advantage of the transient grating technique [20]. In transient grating spectroscopy, a spatially periodic modulation of the dielectric constant can be induced in a material by directing two pulses into the sample to create an interference pattern in that material. This interference pattern creates a change in the dielectric constant at the high intensity fringes, and this results in the build up of a density grating due to either electrostriction of thermal absorption (or both in some cases) induced by the high intensity fringes. In the case of ISBS, the density grating propagates as an acoustic mode which can be probed with the application of a second laser.

The transient grating spectroscopies became known by the name impulsive stimulated light scattering (ISS) in the 1980s when the theoretical framework was developed and published by Keith Nelson and his student Yong-xin Yan [21,22]. In this way, the nomenclature of the ISS technique can be changed to properly describe the excited mode in the experiment: impulsive stimulated Brillouin scattering (ISBS) for when acoustic modes are excited, impulsive stimulated Raman scattering (ISRS) when optical modes are excited, and impulsive stimulated thermal scattering when a thermal grating is produced due to a weak absorption of the pumps by the material [19]. Furthermore, the condition that makes ISS techniques “impulsive” is that the temporal length of the pump pulses must be shorter than one cycle of the wave of interest [21]. This allowed for the excitation force to be described approximately as a δ-function in the development of ISS theory. As an example of meeting the “impulsive” condition, if the expected frequency of the signal was on the order of $f = 100\,MHz$, such as for liquid samples in ISBS experiments [23], one acoustic cycle (or period, T) would be on the order of $T = 1/f = 10\,ns$. A nanosecond pulsed laser would be sufficient to satisfy the impulsive condition in this example.

Figure 1.3 displays a step-by-step depiction of the principle of ISBS. First, two pump pulses are propagated into a medium with an intersecting angle of $2 * \phi_{pump}$ between the two pulses. As the two pump pulses converge within the medium, an interference pattern is produced that modulates the dielectric properties at the interference fringes of high intensity. This temporary grating that is produced in the medium has a fringe spacing (d) given by Equation 1.11.

$$d = \frac{\lambda_{pump}}{2\sin(\phi_{pump})} \tag{1.11}$$

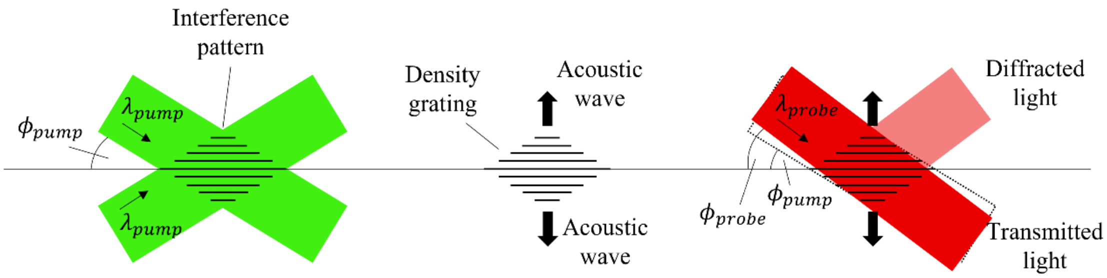

Figure 1.3 The principle of ISBS illustrated from left to right. First two pump pulses intersect and form an interference pattern. The interference pattern induces a density grating and thus an acoustic wave in the medium. The probe beam scatters off this grating and the diffracted light is measured. Adapted from [24].

Here, λ_{pump} is the wavelength of the pump pulse, and ϕ_{pump} is the angle between the pump pulse and the propagation axis. The grating is then probed with a continuous wave (CW) probe laser where part of the probe is diffracted by the grating and intensity modulated by the acoustic frequency. If the signal is generated from (1) a thermal excitation or (2) an electrostrictive excitation with a heterodyne detection scheme, the modulation frequency ($f = f_1$) will be given by Equation 1.12.

$$f_1 = \frac{v_s}{d} = 2\frac{v_s}{\lambda_{pump}}\sin(\phi_{pump}) \tag{1.12}$$

Here, v_s is the speed of sound in the material. If the signal is generated by an electrostrictive excitation with a homodyne detection scheme, the modulation frequency ($f = f_2$) will instead be given by Equation 1.13.

$$f_2 = \frac{2v_s}{d} = 2f_1 \tag{1.13}$$

Further discussion on these signal generation processes, as well as the effect of homodyne/heterodyne detection on the electrostrictive signal, has been detailed in recent work [24,25].

2. FILAMENTATION IN ATMOSPHERIC AIR WITH TUNABLE 1100-2400 NM NEAR-INFRARED FEMTOSECOND LASER SOURCE*

2.1. Introduction

Laser induced filamentation is a nonlinear optical effect where intense laser pulses undergo self-focusing from the Kerr effect to overcome pulse diffraction and to propagate distances much larger than the diffraction length while maintaining a narrow beam diameter. Laser induced filamentation has been observed in solid, liquid, and gaseous media and has been studied in relation to high harmonic generation, supercontinuum generation, and as a method to generate single cycle and attosecond laser pulses [10,26,27]. Of particular interest is understanding open-air pulse propagation and atmospheric filamentation. Atmospheric filamentation provides applications such as atmospheric and remote sensing with techniques such as laser-induced breakdown spectroscopy [28] and white light continuum ranging [29]. Atmospheric filamentation has also been studied as a method to achieve long distance optical communication and transmission of energy [30].

Filamentation occurs when a high power, femtosecond laser pulse propagates through a medium and is self-focused (Kerr lensing) by the intensity dependent refractive index (n_2). If the pulse power (Equation 2.1) exceeds a critical power threshold (Equation

---

* Reprinted with permission from "Filamentation in Atmospheric Air with Tunable 1100-2400 nm Near-Infrared Femtosecond Laser Source" by S. P. O'Connor, C. B. Marble, D. T. Nodurft, G. D. Noojin, A. R. Boretsky, A. W. Wharmby, M. O. Scully, and V. V. Yakovlev, 2019, Sci. Rep., **9**, 12049, Copyright 2019 by Springer Nature. (Reference [123])

2.2) the self-focusing will overcome the pulse diffraction causing the beam to collapse until multi-photon ionization occurs. The critical power threshold is dependent on the nonlinear refractive index ($n_2 \sim 5 \times 10^{-19}\ cm^2/W$ for air [31]) and a numerical factor (C) related to the beam shape ($C \approx 3.77$ for a Gaussian beam, $3.72 < C < 6.4$ in general [16]).

$$P_{Exp} = K\frac{Energy}{Time} \ , \qquad K = 0.94 \text{ for a Gaussian beam} \tag{2.1}$$

$$P_{crit} = \frac{C\lambda^2}{8\pi n_o n_2} \tag{2.2}$$

Plasma generation halts beam collapse. Defocusing from plasma generation balances self-focusing effects which results in the generation of one or more thin filaments of light which propagate distances that are orders of magnitude greater than the Rayleigh range without defocusing [30]. Laser filaments can display unusual properties such as pulse temporal self-compression. Self-compression during filamentation can reshape and shorten the time profile of the pulse leading to potential applications in attosecond pulse generation [27].

Spectral broadening also accompanies filamentation through nonlinear effects such as self-phase modulation and self-steepening which modulates the initial pulse's spectrum into a supercontinuum composed of a broad range of wavelengths. Supercontinuum generation was first reported in 1970 in which 530 nm picosecond pulses were propagated through bulk BK7, and the resulting pulse was spectrally broadened to a 400-700 nm spectral range [26]. Since then, intense "white-light" continuums generated in filamentation and supercontinuum studies have found a broad spectra of applications including optical coherence tomography [32], colorimetry [33], STED microscopy [34], pump-probe spectroscopy [35,36], and Raman spectroscopy [37–40].

The first observation of laser filamentation in air was by Braun *et al.* with a 775 nm input pulse [41]. Since then, atmospheric filamentation has been reported at many wavelengths shorter than 1030 nm and in the mid-IR at 3.9 µm (see Table 2.1). Filamentation with a near-IR input beam has been demonstrated in highly-pressurized gases [42–45]. To our knowledge, filamentation in atmospheric air with a tunable near-IR laser source has not been attempted.

Table 2.1 Filaments in air observed in literature. Critical powers are estimated with Equation 2.2 using $n_2 \sim 5 \times 10^{-19}$ cm^2/W as an estimated from literature [31], and experimental pulse powers are computed with Equation 2.1 assuming a Gaussian pulse.

Wavelength (nm)	FWHM Time Duration (fs)	Pulse Energies (mJ)	Critical Power (C=3.77) (GW)	Critical Power (C=6.4) (GW)	Experimental Pulse Powers (GW)	Reference
248	450	2 – 5	0.2	0.3	4 – 10	[46]
248	5000	7.5	0.2	0.3	1.4	[46]
400	~ 60	2.3	0.5	0.8	36	[31]
406	40	1	0.5	0.8	7	[47]
527	900	1.6 – 4	0.8	1.4	2 – 4	[48]
775	200	2 – 50	1.8	3.1	9 – 235	[41]
800	42	2.3	1.9	3.3	51	[31]
1030	200	1.5 – 10	3.2	5.4	7 – 47	[49]
3900	~ 80-200	20 – 30	46	77	200 – 350	[16]
10200	3500	5200	310	530	1400	[50]

Despite the use of open-air high-power lasers, the eye safety implications of supercontinuum generation in air have not been studied. Eye safety standards such as ANSI Z136.1 set maximum permissible exposure (MPE) limits based on the laser wavelength and time duration, but they do not account for nonlinear processes altering the laser wavelength [51]. Concurrent studies of high harmonic generation in zinc selenide have shown the generation of sufficient visible and near-infrared radiation light from mid-IR source wavelengths to pose a retinal hazard by ANSI standards [52]. Eye safety standards inform the choice of laser eye protection (LEP) used by laser operators who choose LEP that absorbs or reflects the laser wavelength with the minimum reduction of visual acuity and color perception. Filamentation and supercontinuum generation raise the risk of new or additional eye safety hazards being generated during laser operation at wavelengths outside the operating laser wavelength [53]. If LEP is chosen that does not also provide adequate protection against the constituent wavelengths of the supercontinuum, a retinal injury could occur. One possible eye hazard is the production of sub-1050 nm wavelengths which have lower exposure limits compared to >1200 nm pulses since longer wavelength pulses (particularly >1400 nm pulses) are strongly absorbed in the aqueous and vitreous humors of the eye prior to reaching the retina [51].

We demonstrate filamentation in atmospheric air in the lab with tunable near-infrared laser pulses with wavelengths ranging from 1100 nm to 2400 nm. We report the spectrum of the resulting supercontinuum generation as it is projected onto a sheet of paper by measuring the center and fringes of its output for different source wavelengths in increments of 100 nm. The input energy for each source wavelength is measured prior to filamentation. The experimental setup is then modified to collect and record the energy of the visible component of the pulse. We measure the output energy in the sub-1000 nm regime following filamentation for the source wavelengths 1100nm to 1600 nm. We show that filamentation of the input pulse results in intense visible light generation due to both harmonic generation and supercontinuum generation. In some instances, the visible light generation exceeded the MPE values set by the ANSI laser eye safety standard confirming that near-IR pulse filamentation can generate visible eye hazards.

2.2. Methods

Nominally 100 fs near-IR pulses with a source wavelength ranging from 1100 nm to 2700 nm were produced using a High Energy TOPAS optical parametric amplifier (OPA, model TH8F1) and a Spectra Physics® Spitfire Ace regenerative amplifier (model 8PTFPA-100F-1K-ACE) following the design of previous studies [54,55]. Pulses from 1100 nm to 1600 nm were generated using the OPA's signal beam, and pulses from 1600 nm to 2700 nm were generated using the OPA's idler beam. A flip mirror (labeled Au-FM in Fig. 2.1(a)) was used to select either the signal or idler beam as the filamentation source, and the beam diameter ranged from 6 mm to 9 mm depending on the selected wavelength. The beam passed through a 1000 nm long pass filter (Thorlabs® FGL-1000, labeled L in Fig. 2.1(a)) to eliminate extraneous visible light that was emitted from the OPA. A collection of neutral density filters (labeled F in Fig. 2.1(a)) attenuated the beam energy, and the beam was focused in air using a +75 mm calcium fluoride converging lens (labeled L1 in Fig. 2.1(a)) which resulted in filamentation. The chirp from quadratic and cubic dispersion due to the optics was computed [56]. The quadratic dispersion (linear chirp) was found to be positive, but negligible for all wavelengths. The cubic dispersion from the neutral density filters was found to be nonnegligible (and negative) only for 1100 nm and 1200 nm measurements. The supercontinuum generated during filamentation was projected onto a blank sheet of paper. For each wavelength, the supercontinuum spectra were recorded for three pulse energies using three spectrometers. Two spectrometers were pointed at the center of the supercontinuum, one recording the visible spectrum (V1), an Ocean Optics® USB 2000+, and one recording the infrared spectrum (IR1), an Ocean Optics® NIR-512. A second Ocean Optics® USB 2000+ spectrometer was used to record the visible fringe of the supercontinuum (V2).

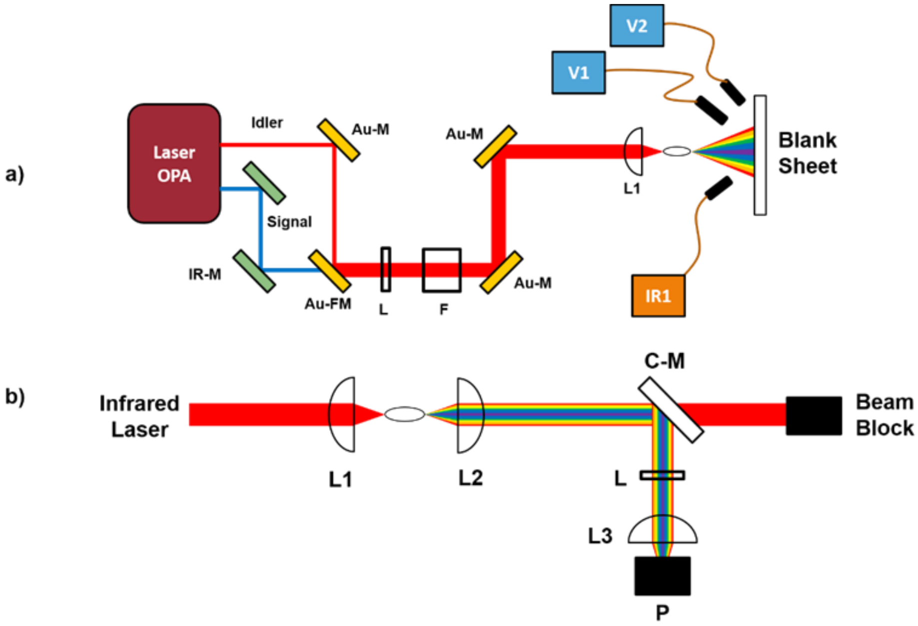

Figure 2.1 a) The experimental setup to observe the supercontinuum generation. b) Removed blank sheet for spectral collection and added optics for visible light collection and power measurement after supercontinuum generation. Au-FM: Gold flip mirror. Au-M: Gold mirror. C-M: Cold Mirror. F: Filter wheel. IR-M: Infrared mirrors. L: Long-pass filter. L1, L2, L3: Converging lenses. P: Power meter. V1, V2: Visible spectrum spectrometers. IR1: Infrared spectrum spectrometer.

The experimental setup was then modified into a collection regime so that the visible light generated during filamentation of the signal beam was focused down and collected (see Fig. 2.1(b)). A +200 mm focusing lens was used to collimate the center of the supercontinuum pulse, and the collimated beam was reflected off a cold mirror (labeled C-M in Fig. 2.1(b)) to remove the near-infrared component of the beam. The reflected light was measured using a power meter (Coherent® PM10, P in Fig. 2.1(b)) with and without a 1000 nm long pass filter (Thorlabs® FGL-1000) in the path of the reflected beam. A 1-inch diameter, BK7 lens (labeled L3 in Fig. 2.1(b)) decreased beam width to fit the sub-1000 nm light onto the power meter. After taking measurements for all source beam wavelengths from 1100 nm to 1600 nm in increments of 100 nm, the +200 mm collection lens was replaced with a +100 mm collection lens and the measurements of reflected light with and without the long pass filter were repeated. To account for the absorption of infrared light due to the 1000 nm long-pass filter, the absorption spectra for the long pass filter from 200 nm to 1600 nm was measured using a spectrophotometer (Cary 6000i, Agilent®). We calculated the energy of the sub-1000 nm component of the output pulse and the conversion efficiency of filamentation after accounting for the absorption due to the long pass filter.

The relative efficiencies at each wavelength were determined for the NIR-512 and USB 2000+ spectrometers using the LS-1 Tungsten Halogen lamp light source (Ocean Optics®). For each spectrometer, the LS-1 was coupled to the spectrometer using the same fiber used in the filamentation experiment and the LS-1 spectrum was recorded. The relative efficiencies were then calculated by comparing the experimentally measured LS-

1 spectra against the expected LS-1 spectra of a 3100 K blackbody. The relative efficiencies were then used to correct the intensity response from our recorded spectral data.

2.3. Results and Discussion

Using the setup in Fig. 2.1, filamentation was achieved for wavelengths ranging from 1100 nm to 2400 nm. For each wavelength, the supercontinuum projected onto the paper was photographed (see Fig. 2.2). In addition to photographing the spectra, the visible and near-IR spectra were recorded by three spectrometers as shown in Fig 2.1(a). From visual examination and spectrometer measurements, the center of the supercontinuum was observed to consist of the fundamental infrared wavelength and third harmonic light. Consistent with previous explorations of conical emission from supercontinuum generation in air, the fringes of the supercontinuum were observed to consist of supercontinuum broadened light with larger conic emission angles corresponding to shorter (visible) wavelengths [57,58]. In this experiment, the fringes were generally less intense than the third harmonic light, with the exception of the measurements taken with source wavelengths at 1300 nm and 1400 nm (see Fig. 2.2(a) and (b)).

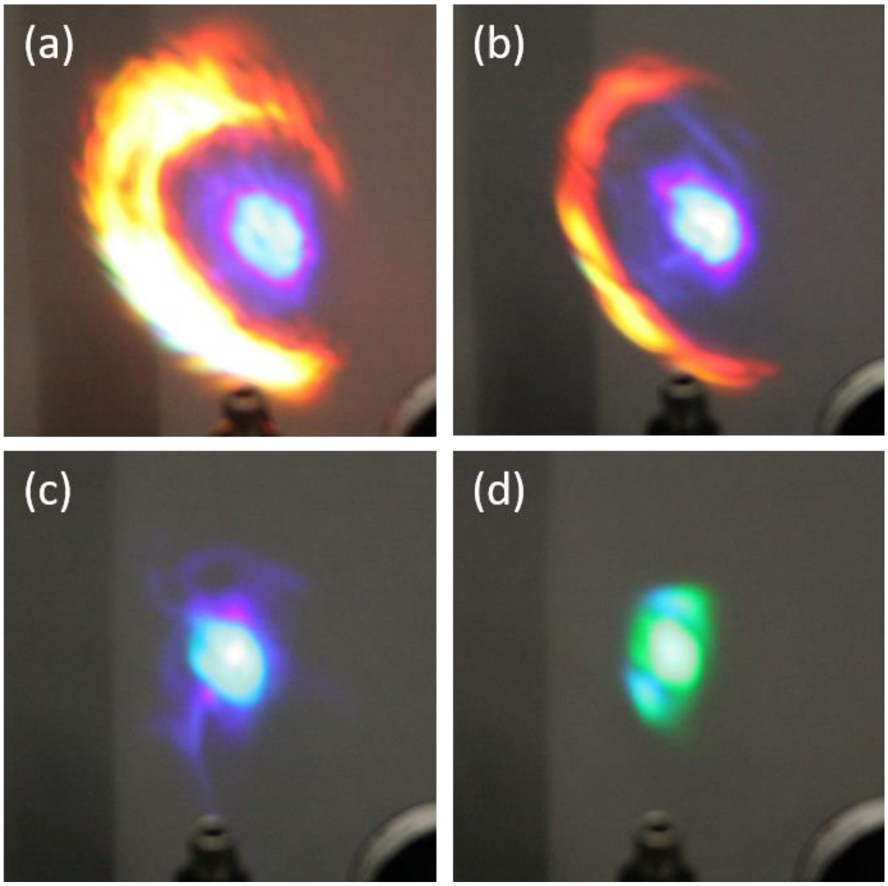

Figure 2.2 Supercontinuum generation imaged onto a sheet of blank white paper. Source wavelength for each continuum is (a) 1300 nm (b) 1400 nm (c) 1500 nm (d) 1600 nm.

The measured wavelengths for the third harmonic peaks are reported in Table 2.2, along with the predicted third harmonic wavelength for each source wavelength. We find that our wavelength measurements for the observed third harmonics were within 6% of the predicted wavelength values. We also report the supercontinuum spectral ranges we measured from each spectrometer in Table 2.2. Beam diameters for the 1100 nm and 2400 nm sources were not acquired as the maximum pulse energy was too weak to detect with the beam camera.

Table 2.2 Beam parameters for spectra generation. Wavelengths followed by "-I" were generated using the Idler beam. Acronyms: Not Measurable (NM), Not Observed (NO).

Wavelength (nm)	Max Pulse Energy (μJ)	Beam Diameter (mm)	Supercontinuum Range 1 (nm)	Supercontinuum Range 2 (mm)	Predicted 3rd Harmonic (nm)	Observed 3rd Harmonic (nm)
1100	210 ± 30	NM	1030-1130	NO	367	352
1200	740 ± 60	7.5	980-1230	615-850	400	389
1300	840 ± 60	7.6	1015-1355	660-870	433	431
1400	1530 ± 20	6.9	1145-1430	595-860	467	464
1500	1360 ± 60	7.0	1285-1575	NO	500	498
1600	1180 ± 20	6.5	1475-1675	NO	533	530
1600-I	1220 ± 20	7.3	1200-1685	670-870	533	529
1700-I	1420 ± 40	8.7	1220-1720	545-840	567	559
1800-I	1025 ± 6	8.4	1445-1705	655-870	600	604
1900-I	1185 ± 8	9.8	1520-1720	NO	633	635
2000-I	970 ± 7	9.1	1565-1715	NO	667	681
2150-I	885 ± 4	8.3	NO	NO	717	757
2200-I	980 ± 20	8.5	NO	NO	733	734
2300-I	684 ± 8	7.8	NO	NO	767	784
2400-I	47 ± 4	NM	NO	NO	800	813

Spectra measured from the blank sheet of paper are shown in Fig. 2.3. We observed supercontinuum generation in the visible and in the infrared regimes, and this light was at least an order of magnitude greater than the noise floor in Fig. 2.3. Distinguishable third harmonic generation peaks can be seen on each figure at the wavelengths that are listed in Table 2.2. We observed spectral broadening of the pump pulse's wavelength along with the development of a spectral lobe similar to previous studies in highly pressurized gas [43–45]. We find that the spectral lobe is blue-shifted with respect to the pump pulse's central wavelength.

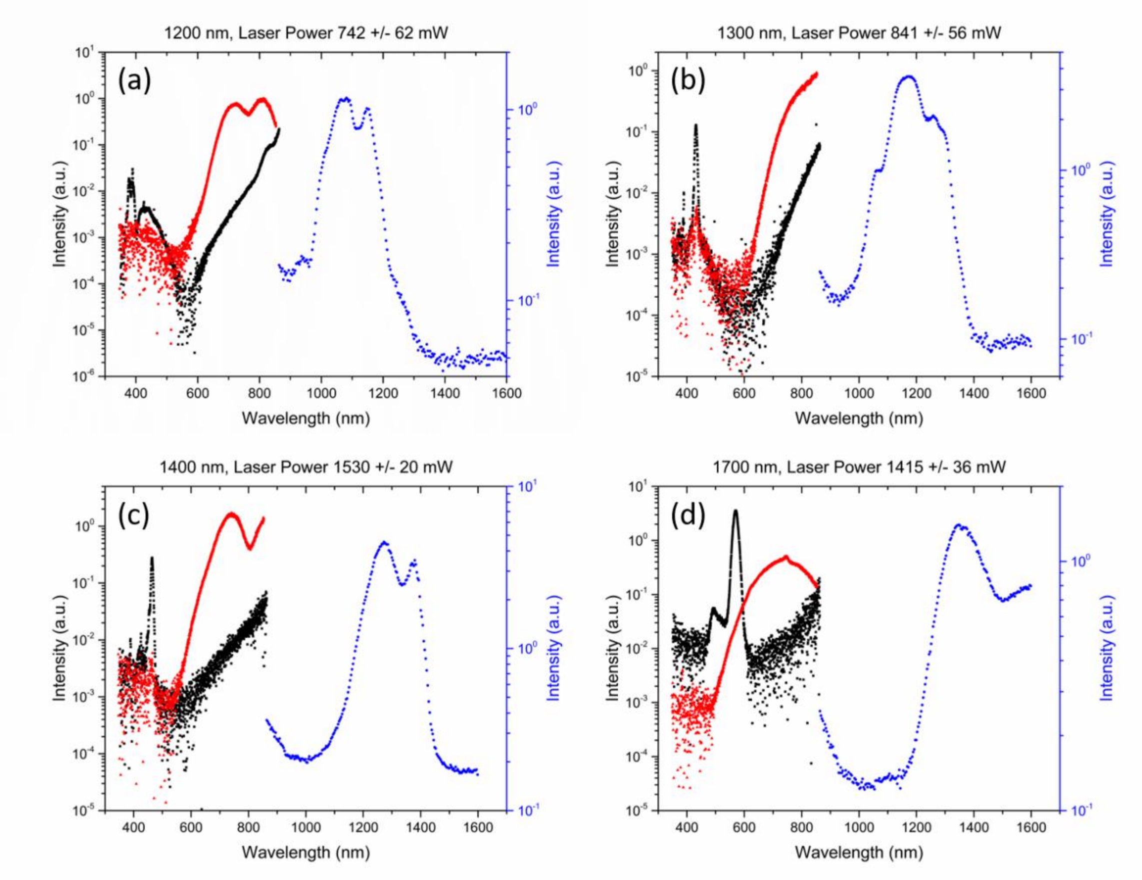

Figure 2.3 Supercontinuum spectra of the center (black) and fringes (red) of the visible output as well as the center output of the IR (blue) are shown above. The left axis corresponds to the visible light data, and the right axis corresponds to infrared data. Source wavelengths shown are (a) 1200 nm (b) 1300 nm (c) 1400 nm (d) 1700 nm. Intensities shown were corrected using the relative efficiencies from the LS-1 light source.

Having recorded the spectra of the supercontinuum generation, we then measured the pulse energy using the setup in Fig. 2.1(b) with and without the FGL-1000 long pass filter. By measuring the energy with and without the long pass filter and correcting for the infrared wavelength loss of the long pass filter, the sub-1000 nm pulse energy was determined for the +200 mm lens setup and +100 mm lens setup (Fig. 2.4). In both configurations, 1300 nm and 1400 nm wavelengths were observed to generate micro-Joules of sub-1000 nm radiation, which is a clear eye hazard based on the ANSI limits and input beam radius. If the 1300 nm beam was recollimated to a beam diameter of 7.6 mm, the sub-1000 nm light energy per unit area would approach (30.4 ± 1.8) μJ/cm^2, exceeding the ANSI limit of 0.1 μJ/cm^2 by two orders of magnitude [51]. These results agree with visual observations of the supercontinuum at 1300 nm and 1400 nm which were intense even when scattered from a piece of paper (Fig. 2.2(a) and (b)). The +200 mm experiment suggests that the 1600 nm filament was a visible eye hazard while the +100 nm lens setup suggested that the 1500 nm filament was a visible eye hazard. Both setups failed to collect the entire supercontinuum spectra. The +200 mm lens was only able to capture the center, third harmonic region, of the continuum resulting in lower reported pulse energies.

2.4. Conclusion

We performed a systematic study of near-IR filamentation in atmospheric air using femtosecond pulses with source wavelengths ranging from 1100 – 2400 nm. We demonstrated that these near-IR wavelengths were able to generate a supercontinuum in the visible spectrum, as well as distinct third harmonics. Measurements of the spectrum exhibited a strong third harmonic response that appears within the visible light spectrum for most of our input wavelengths, with the exception of near-IR third harmonics for >2000 nm source wavelengths.

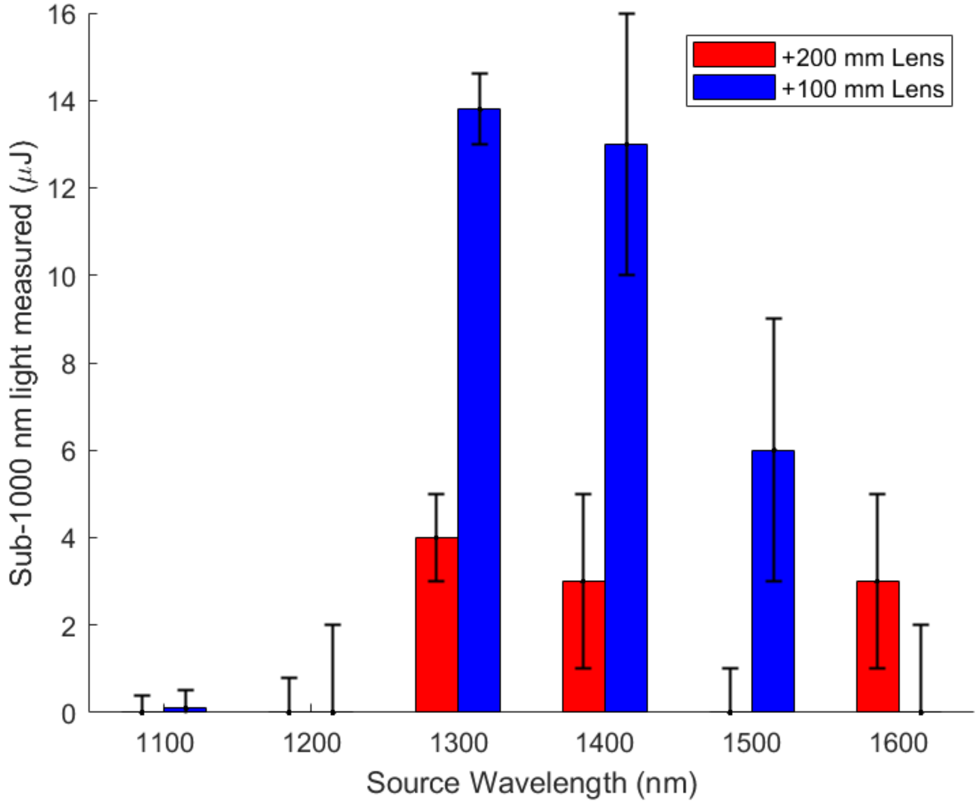

Figure 2.4 Sub-1000 nm light generation collected from power meter (P) in the experimental setup in Fig. 2.1(b). Input pulse energy for each source wavelength is the max pulse energy listed in Table 2.2. The starting beam diameter of each pulse is also listed in Table 2.2.

These third harmonic peaks in the visible light spectrum demonstrate a clear laser-eye safety hazard according to the ANSI guidelines [51]. The generation of sub-1050 nm infrared third harmonic light for >2000 nm source wavelengths is worrisome from an eye safety perspective, because laser operators would observe an intense, visible pulse for shorter source wavelengths. However, they would not be aware of their exposure to sub-1050 nm infrared harmonics and continuum for >2000 nm wavelengths. The supercontinuum and high harmonic generation from the ultrashort pulses need to be taken into consideration in applications of atmospheric filamentation. In particular, the infrared laser eye protection worn to protect against exposure to the source wavelength may not provide sufficient protection against the third harmonic wavelength.

Further study of near-IR filamentation is necessary to determine the hazard that is posed from supercontinuum and harmonic generation in the infrared regime, because the 1000-1200 nm infrared energies were not recorded in the collection setup (Fig. 2.1(b)) of our study. For some of our source wavelengths, we observed that supercontinuum generation occurs in the near-IR regime which can propagate to the back of the retina, and we note that >2000 nm pulses generate spectra located almost entirely in the near-IR. Quantification of this 1000-1200 nm near-IR generated light is essential to understanding the risk to laser-eye safety that atmospheric air pulse propagation and filamentation can pose. Furthermore, the strong nonlinearity of the supercontinuum and harmonic generations in atmospheric air propagation indicate that the resulting spectral output is subject to large variations from changing the experimental parameters, such as the focal length and atmospheric conditions. Future work characterizing sub-1050 nm generation efficiencies from nonlinear processes with fine control of source pump energy and examining a worst-case analysis will be necessary to provide specific protection recommendations for laser-eye safety.

3. TRANSIENT ABSORPTION SPECTROSCOPY TO EXPLORE CELLULAR PATHWAYS TO PHOTOBIOMODULATION[*]

3.1. Introduction

Photobiomodulation (PBM) utilizes low irradiance light in the red to near-infrared (NIR) wavelength range (R-NIR) to generate beneficial biological effects in living cells and tissues. One early study of PBM showed that exposing cells to a low-power 632.8-nm HeNe laser stimulated ATP synthesis in mitochondria [59]. Since then, a wide range of methodologies have been used to study the effects of PBM, ranging from biological methods such as histology [60] and western blot analysis [61], to the techniques of spectrophotometry [62], Raman spectroscopy [63], and fluorescence [64]. Many of these studies focus on the products, or downstream effects of cellular processes, rather than the immediate photon absorption steps by proteins that initiate the PBM processes. Some beneficial physiological outcomes from PBM include enhanced wound healing [65,66], pain relief [67,68], cell proliferation [69], and reduction of both inflammation [70] and muscular soreness [71], as well as increased muscular performance, resistance to muscle fatigue [72], nerve regeneration [73–75], and mitigation of traumatic brain injury [76].

Mitochondria, the chief producers of ATP in eukaryotic cells, are generally accepted as critical targets of PBM therapy [77]. The leading hypothesis for the origin of

---

[*] Reprinted with permission from “Transient absorption spectroscopy to explore cellular pathways to photobiomodulation” by S. P. O’Connor, S. M. Powell, J. M. Rickman, N. J. Pope, G. D. Noojin, M. O. Scully, M. L. Denton, and V. V. Yakovlev, 2021, J. Photochem. Photobiol. B Biol., **222**, 112271, Copyright 2021 by Elsevier B.V. (Reference [103])

the PBM effect points specifically towards an enzyme complex in the electron transport chain (ETC). The absorption profile of Complex IV (C-IV) has several similarities with the action spectrum for PBM and has been named the primary photoreceptor for PBM therapies [78–83]. However, other ETC proteins, namely Complex III (C-III) and cytochrome c (Cyt c), share some of the absorption properties of C-IV, and are often found bound together in multimeric supercomplexes. Therefore, it is important to widen the focus of PBM research to include C-III and Cyt c as potential targets of PBM therapies.

The primary role of Cyt c in the ETC is to shuttle electrons between C-III and C-IV, and in the process, pump protons across the mitochondrial membrane to contribute to the electrochemical proton gradient that drives the synthesis of ATP [84,85]. C-III, C-IV, and Cyt c are heme-containing proteins. Heme groups are iron-containing porphyrins whose absorption spectra are characterized by a strong absorption peak in the Soret band (~380 - 500 nm), and weaker absorption peaks in the Q band (~500 - 700 nm) [86]. The ability of these proteins to shuttle electrons, in combination with the fact that heme proteins are easily characterized by spectroscopic techniques [86], also make C-III, C-IV, and Cyt c potential candidates for involvement in PBM. Thus, light-dependent perturbations in the electronic transitions of these three photoactive proteins would implicate them in the initiation of PBM pathways.

Light-induced electronic excitations in proteins can be on the order of femtoseconds (fs) to picoseconds [87,88], thus requiring the use of a femtosecond laser source to obtain the necessary temporal resolution for resolving these dynamics with spectroscopy. Ultrafast spectroscopic methods, such as fs transient absorption spectroscopy (TAS) are ideal for studying short-lived photoinduced energy and electron transfers, such as those expected at the beginning of the signaling pathways associated with PBM. Applying light exposures, consistent with those used in PBM studies to individual ETC proteins during TAS data collection, could eliminate or implicate these proteins for involvement in the PBM response.

TAS is a pump-probe spectroscopic technique that can characterize the photophysical dynamics of biological and chemical systems. In TAS, if the sample contains molecules that absorb photons at the pump wavelength, a single ultrashort pulse from the pump promotes a fraction of the chromophore's electrons into a transient excited state. At various delay times relative to the pump pulse [18], a single probe pulse of supercontinuum light provides a broadband absorption measurement of the sample. Typically, both the pump and probe pulses have durations of about 100 fs. As the time delay is varied, and if the transient electronic states have a unique absorption wavelength relative to the ground state absorption profile, the method identifies absorption lifetime dynamics that are specific to the chromophore and type of photoproduct generated. This process is repeated multiple times, changing the time delay each time, until all transients have either transferred their energy or decayed back to the ground state.

To normalize the transient spectra, the pump probe is delivered at one-half the frequency of the probe pulses, and those absorption measurements without a preceding pump pulse make up the dynamic ground state absorption spectra. In real time with the probe pulses, the ground state absorption value (without pump) is subtracted from the excited state absorption (with pump pulse preceding) to obtain an absorbance difference

(ΔA) at each delay time. Over the course of the measurement, a complete ΔA profile, as a function of both wavelength and time delay (ΔA(λ, t)), is generated.

Even though there is a generally accepted hypothesis for the PBM process that begins with electronic transitions in C-IV [78,80], others have reported the possibility of a photophysical mechanism whereby R-NIR light reduces intracellular water viscosity [89]. Addressing the question of an electronic excitation mechanism, we have modified the TAS method to include a third laser beam incident on the same sample volume interrogated by the pump and probe beams. Here, this third beam has wavelength and irradiance (W/cm^2) dosimetry consistent with those giving rise to release of nitric oxide (NO) in retinal pigment epithelial cells in culture [64]. Whether this release of NO is an early step in the path to PBM remains unknown, but neither NO release nor PBM effects occur immediately upon exposure to light. This implies a delayed metabolic response. Thus, when looking for immediate light-induced effects in purified proteins, or even isolated mitochondria, we are cautious about calling the applied low-irradiance CW light a “PBM light” because this would imply a known down-stream effect. Our new TAS configuration allowed us to perform TAS in real time with low-irradiance exposures, during the accumulation of radiant exposure. Although TAS has been used to probe the excited state dynamics of C-III [90,91], Cyt c [92–94], and C-IV [95], none of these studies assessed the effects an additional beam of light in real time with TAS data collection, such as R-NIR low-irradiance light.

In this study, we describe a modified TAS method that combines a 532-nm pump beam, a 350-600 nm supercontinuum probe, and an experimental beam of varying continuous wave (CW) irradiances at either 450 nm, 635 nm, or 808 nm to interrogate Cyt c in its reduced form. The focus of this study will be on Cyt c because it is a much smaller and less challenging protein to work with than C-IV, thus allowing us to establish a proof of concept for future studies focusing on C-IV. Because PBM effects at the system level require a certain time of exposure, our hypothesis is that capturing successive TAS data in real time with the CW laser will capture a time-dependent "switch" in the electrodynamics of the purified photoactive proteins that are suspected of being responsive to the CW wavelength. In this manner, we also demonstrate that this concomitant CW exposure does not degrade or interfere with the TAS signal. We believe the described method to be useful in characterizing photoresponsive proteins or enzyme complexes. The application of this technique, which we call CW-TAS, to the components of the ETC will allow us to identify whether R-NIR low-level light can induce electronic transitions in the enzyme complexes implicated in PBM.

3.2. Methods

3.2.1. Sample preparation

Cytochrome c was purchased from Sigma-Aldrich and used without further purification. Samples (0.8 mM) of oxidized cytochrome c (Cyt c_{ox}) were prepared by mixing solid Cyt c in a 25 mM $NaPO_4$, pH 6.3 buffer containing 0.14 M NaCl. To prepare samples of the reduced form (Cyt c_{red}), a small amount of solid dithionite was added to the solution of Cyt c_{ox}. The sample was centrifuged briefly to remove excess solid. The oxidation state of all samples was verified by UV-VIS spectroscopy using a Cary 6000i spectrophotometer prior to all TAS experiments. Samples were assayed in a quartz cuvette with a 2-mm path length.

3.2.2. Transient absorption spectrometer setup

All TAS experiments were performed with a HELIOS Fire (Ultrafast Systems) transient absorption spectrometer, and Figure 3.1 displays a schematic of the HELIOS system. The pump and probe sources were provided by a Ti:sapphire regenerative amplifier (SpitFire Ace, Spectra-Physics) with wavelength centered at 800 nm, pulse duration of 80 fs, and repetition rate of 1 kHz. The pump pulses were generated by splitting part of the 800-nm source light to an optical parametric amplifier (OPA; TOPAS-Twins, Light Conversion), where it was converted to 532-nm light (FWHM ~10 nm) by the method discussed in previous studies [54,55]. The pump light traveled through a chopper wheel (CW, Fig. 3.1) that reduced the repetition rate to 500 Hz. The pump pulses were focused with a converging lens (L1, Fig. 3.1) and directed to be coincident with the probe pulses within the sample (S, Fig. 3.1). The probe pulse consisted of a supercontinuum (350-600 nm) generated from the fundamental 800-nm pulse incident upon a window of CaF_2 (W, Fig. 3.1), also having a repetition rate of 1 kHz. After the supercontinuum probe was generated, the center of the probe beam passed through a through-hole in the first parabolic mirror (PM1, Fig. 3.1) to eliminate the majority of the remaining 800 nm. The remaining annular shaped probe continued to the next parabolic mirror (PM2, Fig. 3.1). This light passed through an 800-nm notch filter (F, Fig. 3.1) to remove the residual 800 nm. The second parabolic mirror redirected and focused the probe pulse into the beam path of the pump pulse. The foci of the pump and probe pulses converged at the same volume within the sample (S, Fig. 3.1), and the annular shape of the probe beam kept it from overlapping with the pump until it reached the sample. After passing through the sample, the pump and probe pulses approached the third parabolic mirror (PM3, Fig. 3.1) with a through-hole which allowed the pump pulse to pass through and collimated the annular-shaped probe pulse. The final parabolic mirror (PM4, Fig. 3.1) focused the probe pulse into the collection fiber (CF, Fig. 3.1). The beam radius of the pump pulse was about 100 μm at its focal point, as determined by the knife-edge technique [96] assuming a $1/e^2$ beam waist.

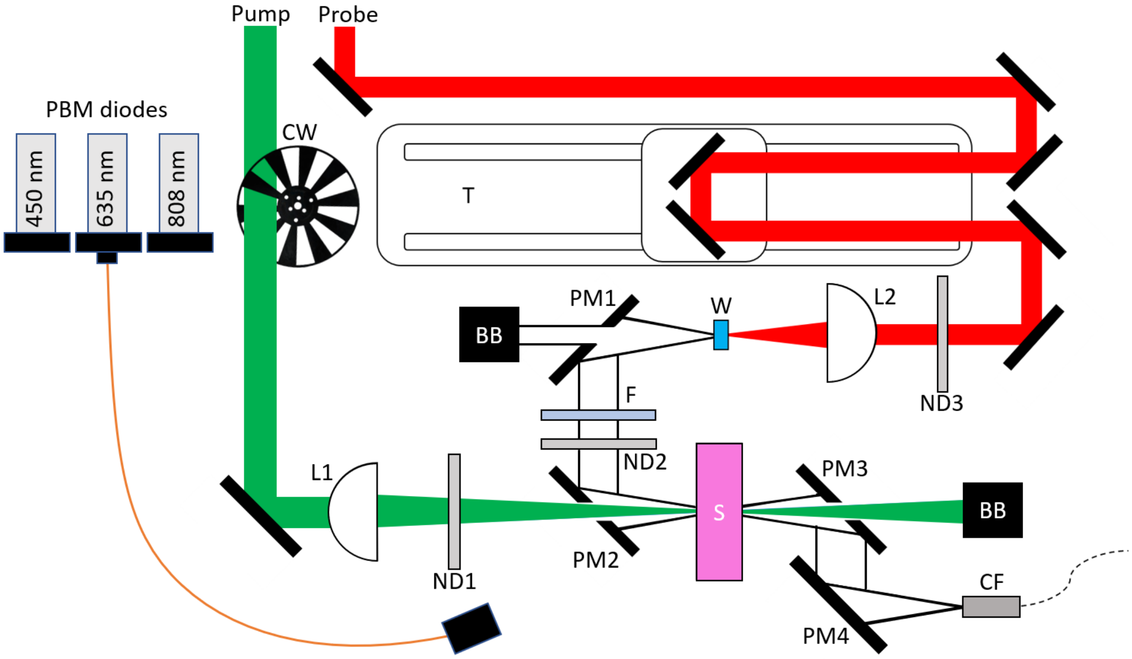

Figure 3.1 Schematic for the HELIOS Fire fs transient absorption spectrometer. BB denotes the beam blocks. CF is the collection fiber connecting to the spectrometer. CW is the chopper wheel. F is the 800-nm filter. PM1, PM2, PM3, and PM4 are off-axis parabolic mirrors. L1 and L2 are converging lenses. ND1, ND2, and ND3 are neutral density filters. S is the sample. T is the translation stage. W is the window of CaF_2.

As shown in Figure 3.2, the CaF_2 window generated a supercontinuum in the ultraviolet to visible (UV-VIS) region. The CaF_2 crystal was kept in motion through translation to maintain the stability of the supercontinuum output and to prevent damage from the incident 800-nm pulses [97].

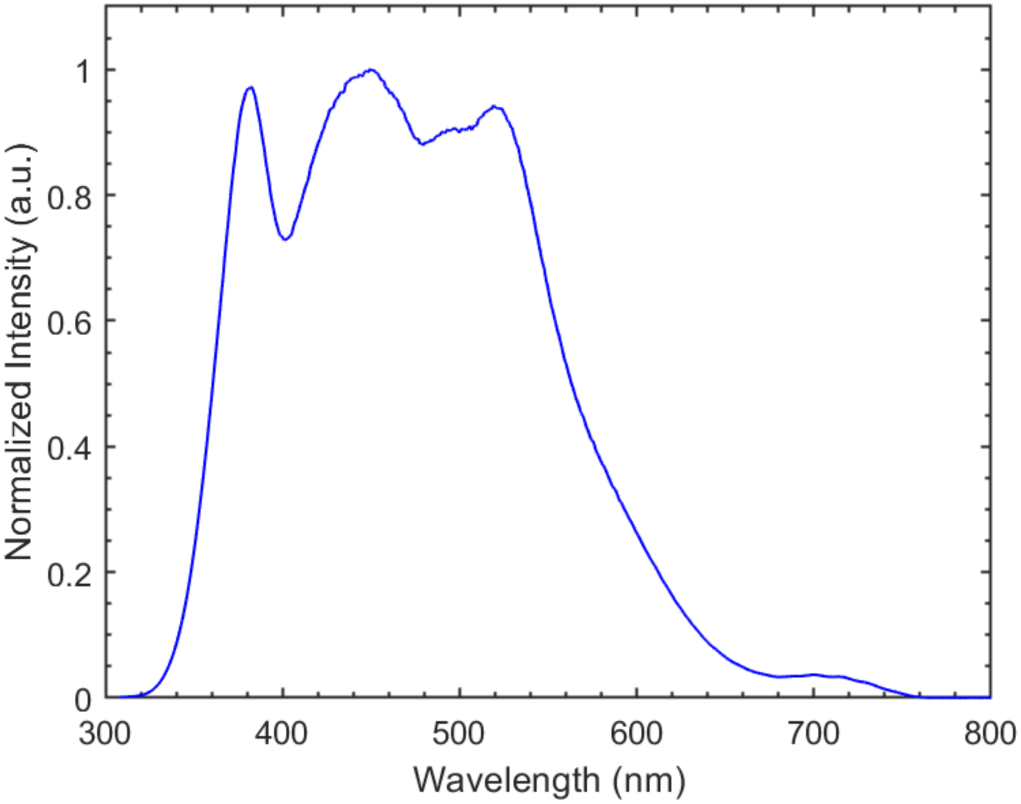

Figure 3.2 Supercontinuum spectra generated from the CaF_2 window.

3.2.3. Low-irradiance CW laser diode setup

For sample irradiation with low-irradiance CW lasers during TAS scanning, the output from one of three laser diodes was coupled into a fiber imaging system (Fig. 3.1) that was mounted in the transient absorption spectrometer. We used CW laser diodes (Thorlabs) with wavelengths of 450 nm (blue; CPS450), 635 nm (red; CPS635), or 808 nm (NIR; CPS808A) that were all interchangeably coupled into a 550-μm diameter fiber (M37L02, Thorlabs). The output power of the diodes was controlled with a continuously variable neutral density filter (NDL-25C-2, Thorlabs) prior to the coupling of the light into the fiber. The fiber output was imaged to the sample with a flat top beam profile having a diameter of 0.95 cm, resulting in an area of 0.71 cm^2 at the cuvette. The fiber output was placed above the pump, probe beam plane, and directed to the cuvette at a shallow angle so that the diode light was not collected by the parabolic mirror (PM3, Fig. 3.1) beyond the sample. The light from the laser diode illuminations did not affect the $\Delta A(\lambda, t)$ spectrum, as verified through observation of the real time $\Delta A(\lambda)$ spectrum in the HELIOS software.

3.2.4. Testing parameters

For the TAS procedure, the 532-nm pump wavelength was used with a power of 15 μW, and the UV-VIS supercontinuum was used for the probe pulse. The pump and probe pulse overlap was optimized before the start of each TAS measurement by testing with a 0.36 mM Rhodamine 6G in methanol solution and maximizing the signal response using the Helios spectrometer. The time delay setup for each scan was programmed to take 0.2-ps steps from -2 to 0 ps, 0.05-ps steps from 0 to 3 ps, 0.1-ps steps from 3 to 10 ps, and 0.5-ps steps from 10 to 50 ps, for a total of 221 time steps. At each time delay step, 0.5 s of measurement were taken, which resulted in 250 $\Delta A(\lambda, t)$ measurements averaged together at that time delay. The TAS program was set to take a total of 14 contiguous time scans for each replicate of Cyt c tested. The first scan was taken as a baseline and did not have any CW laser diode light incident upon the sample. Scans 2-11 were taken with a CW diode emitting light onto the Cyt c sample. Scans 12-14 were taken with the CW diode turned off to observe changes after the full dosage of irradiation [64]. The total time to record 14 scans was 46 min and 36 ± 11 s. The duration of the CW diode exposure during scans 2-11 was computed to be 33 min and 17 ± 8 s. A detailed analysis was done to determine the number of necessary data sets to be collected in order to have a sufficient signal to noise ratio (See Appendix A, section A.1) and it was determined that five sets was sufficient. Five CW-TAS data sets were collected with each laser diode at each irradiance specified in Table 3.1, with the exception of the red laser diode at 3.20 mW/cm^2 where six sets were collected. The visible CW laser studies were conducted individually with an irradiance of either 1.60 or 3.20 mW/cm^2. Exposures at 808-nm were at 1.60 mW/cm^2 due to its maximum power constraint of 2.78 mW/cm^2.

Table 3.1 Laser diode parameters used for CW-TAS of Cyt c samples.

Laser diode	CPS450		CPS635		CPS808A
Irradiance (mW/cm^2)	1.60	3.20	1.60	3.20	1.60
Total Power (mW)	1.13	2.27	1.13	2.27	1.13
Radiant Exposure (J/cm^2)	3.20 ± 0.01	6.39 ± 0.03	3.20 ± 0.01	6.39 ± 0.03	3.20 ± 0.01
Total Energy (J)	2.26 ± 0.01	4.53 ± 0.02	2.26 ± 0.01	4.53 ± 0.02	2.26 ± 0.01

3.2.5. Data processing and analysis

Data was collected and exported from the Helios FIRE software and processed in Surface Xplorer (version 4.3.0, Ultrafast Systems). Background subtractions were performed using the spectra taken at the time delays prior to time-zero. Chirp correction was performed for each data set, and the time-zero correction was acquired by fitting the coherence spiking near the zero delay time in the surface data. CW data sets were processed by averaging together each scan from a replicate sample to the same scan number from other replicate data collections. Then, the averaged baseline data were taken and compared to the averaged scan number 11, when the maximum amount of CW radiant exposure was delivered. Kinetic cross sections were taken at wavelength 374, 415, 430, and 570 nm, and the absorption difference kinetics of the full dosage scan was compared to the baseline kinetics.

Kinetic and global analyses were conducted in Surface Xplorer. Kinetic fits were computed by the software using a sum of exponential decays convolved with a Gaussian instrumentation response function (IRF), as detailed in previous studies [98].

$$C(t) = \exp\left[-\left(\frac{t-t_0}{t_p}\right)^2\right] * \sum_i A_i \exp\left[-\frac{t-t_0}{\tau_i}\right] + A_0 \quad , \quad t_p = \frac{w_{FWHM}}{2\ln(2)} \qquad (3.1)$$

Equation 3.1 displays the kinetic model, C(t), as a function of time (t) between the pump and probe pulses, where $*$ indicates convolution. In the equation, A_i is the magnitude contribution of each exponential decay of time constant (τ_i), t_0 is time-zero, and t_p is a fit parameter relating to the Gaussian IRF's full width at half maximum (FWHM) shown as w_{FWHM}. Global analysis was performed by first performing principle component analysis on surface data through singular value decomposition (SVD) as detailed in previous studies [99]. Equation 3.1 was then used on the selected principal components to acquire the time constants.

3.3. Results

3.3.1. TAS of reduced cytochrome c

TAS measures the absorbance of excited state transitions of electrons, so it is important to first establish the ground state absorbance of the sample. Figure 3.3 presents the ground state absorbance spectra of both reduced and oxidized Cyt c using the Cary spectrophotometer. Cyt c_{ox} had a strong absorption peak in the Soret band at 409 nm, and a single, broad absorption peak in the Q band at 530 nm. The Soret peak for Cyt c_{red} was red-shifted with a λ_{max} at 415 nm, and in the Q band region, there were two peaks at 520 nm and 550 nm. The 532-nm pump's bandwidth (FWHM ~10 nm) overlapped with the absorption peaks of both reduced and oxidized Cyt c and allowed for the excitation of both species. The reduced form of Cyt c was used for all TAS experiments in this study.

There are two possible changes in TAS data that would indicate light-induced electronic transitions had occurred. First is the appearance, disappearance, or a change in wavelength-specific absorption of one or more transient species due to the presence of the low level light. Second is a modification in decay times for a transient species present in the absence of the low-irradiance light. Once a contributing photosensitive protein is found, our analysis will provide valuable feedback for optimizing the dosimetry of the low-level light, and perhaps for the PBM response in general. From this information, we can further elucidate what underlying molecular processes are stimulated through PBM therapies.

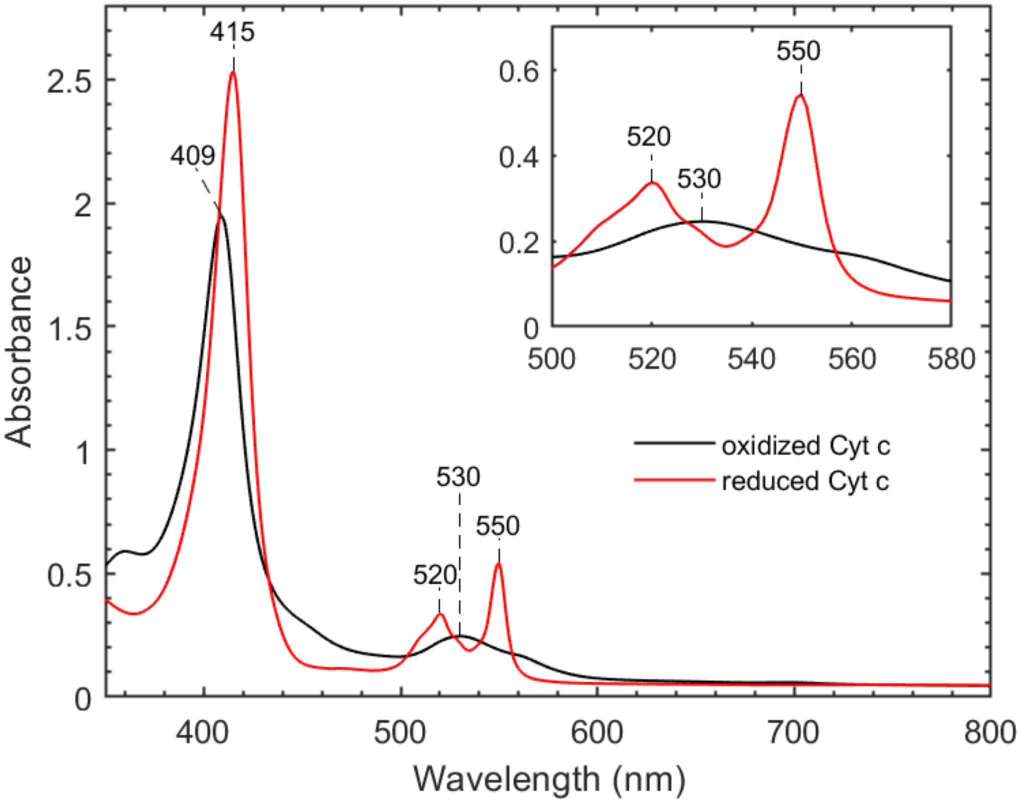

Figure 3.3 Ground state absorbance spectra for Cyt c in its reduced (red) and oxidized (black) states. Inset plot displays a magnified view of the Q band.

TAS data collected for Cyt c in the Soret region using the 532-nm pump is shown in Figure 3.4(a). The surface plot displayed positive transients (orange and red colors) at 374 nm and 429 nm, corresponding to excited state absorptions. More specifically, the 374-nm signal corresponded to changes in the heme δ band and the 429-nm signal corresponded to a ferrous five-coordinated heme [100]. The negative transient signal (blue color) at 415 nm corresponded to ground-state bleaching due to greater Soret band absorbance by Cyt c (Fig. 3.3). TAS data were also collected for the Q band using the 418-nm pump (See Appendix A, section A.2, Fig. A.3), which displayed ground-state bleaching at around 520 nm and 550 nm. Figure 3.4(b) displays spectral cross sections over the Soret and Q bands taken at different time delays with the 532-nm pump scattering region not displayed. The ground-state bleaching at 550 nm was partially resolvable with the 532-nm excitation, but not addressed further in kinetic analysis due to overlap with the 532-nm scattering region. Our TAS spectra agree with previous studies reported for reduced Cyt c [92–94].

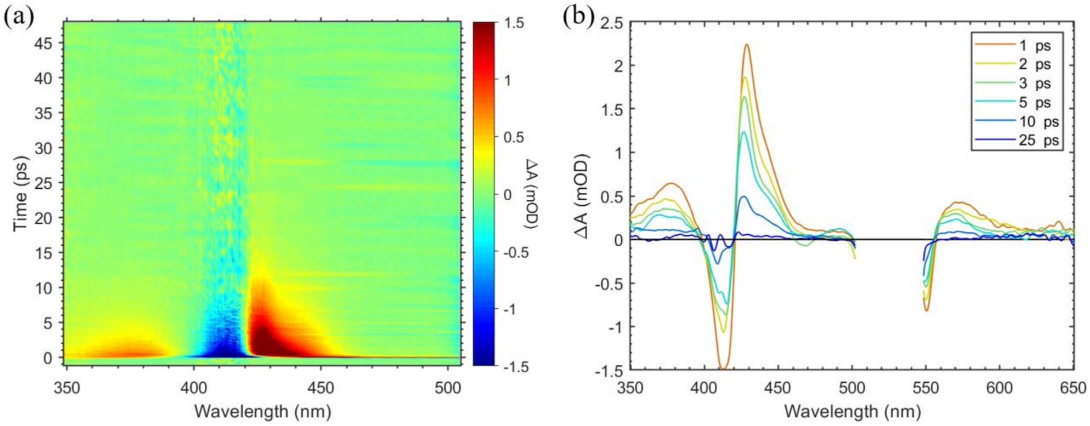

Figure 3.4 Transient absorption spectra of Cyt c with 532-nm excitation at 30 nJ/pulse displayed as (a) a surface and (b) spectral cross sections at different time delays.

3.3.2. CW-TAS comparison results – kinetic analysis

Comparisons between TAS data with and without CW light, made by examining kinetic cross sections of the surface data at wavelengths having observed transients, indicated no differences. Selection of wavelengths at or around local extrema of peaks (transients) and troughs (bleaching) appearing after the coherence spiking near time-zero defined the data for comparison. Averaged kinetic data from the 11th scan with CW light was best for the comparison because this represented the time of delivery for maximum CW radiant exposure. Averaged kinetic data from the samples without CW light exposure provided the baseline for comparison with CW exposure. Figure 3.5 displays the comparisons of kinetic cross sections without and with 635-nm CW exposure at 3.20 mW/cm,^{2} taken at 373.6, 415.1, 429.5, and 569.6 nm. The normalized kinetic cross sections between the control data and CW data showed no significant deviation. Similar results (data not shown) were observed for the other CW wavelengths and irradiance settings listed in Table 3.1.

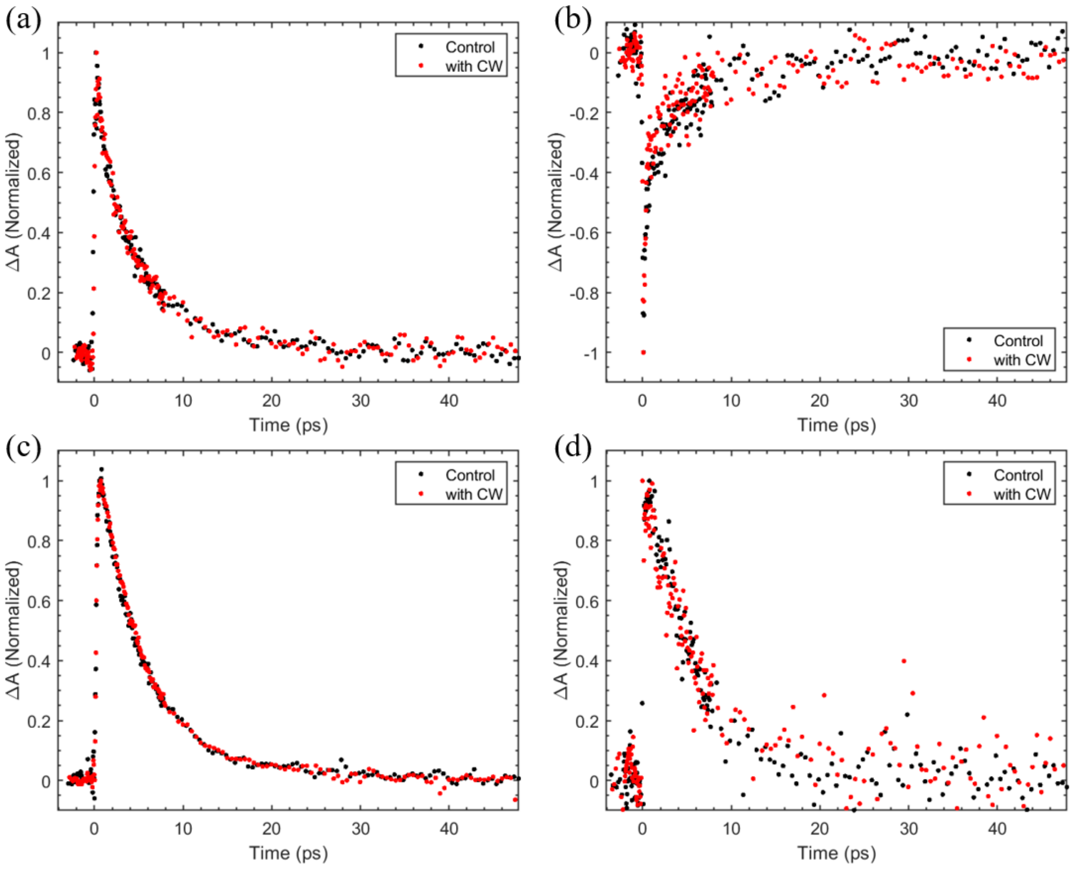

Figure 3.5 Kinetic cross sections of Cyt c TAS data at (a) 373.6 nm, (b) 415.1 nm, (c) 429.5 nm, and (d) 569.6 nm, displaying the normalized transient response both with (red) and without CW (black). Pump power was 30 nJ/pulse, and the CW light was from the 635-nm diode at 3.20 mW/cm^2.

Surface Xplorer provided kinetic fit for the time constants in each cross section shown in Figure 3.5. Table 3.2 provides the compiled time constants, along with their uncertainties as computed at the 90% confidence interval. The time constants extracted from the data with full dosage CW light did not vary in a statistically significant way from the time constants of the data without CW light. This supports the idea that the relaxation and transition processes in Cyt c were not changed by the CW dosages used in this study, and this is further explored with more robustness with global analysis techniques (see section 3.3.3).

Table 3.2 Kinetic fit results for Cyt c. Control sets were calculated with n = 14, whereas CW data sets were calculated with n = 5, except in the case of 635-nm CW at 3.2 mW/cm^2 where n = 6.

Cross-Section Wavelength (nm)	CW Wavelength (nm)	CW Irradiance (mW/cm^2)	τ_1 (ps)	τ_2 (ps)
373.6	Control #1	-	4.4 ± 0.3	-
	Control #2	-	4.7 ± 0.5	-
	450	1.60	4.8 ± 0.5	-
	450	3.20	4.3 ± 0.4	-
	635	1.60	3.9 ± 0.6	-
	635	3.20	4.5 ± 0.3	-
	808	1.60	4.1 ± 0.4	-
415.1	Control #1	-	0.22 ± 0.11	5.6 ± 1.2
	Control #2	-	0.19 ± 0.17	5.4 ± 1.4
	450	1.60	0.19 ± 0.42	4.8 ± 3.0
	450	3.20	0.20 ± 0.15	5.6 ± 2.9
	635	1.60	0.20 ± 0.19	4.8 ± 2.4
	635	3.20	0.23 ± 0.08	5.2 ± 1.8
	808	1.60	0.47 ± 0.38	5.4 ± 2.7
429.5	Control #1	-	0.19 ± 0.09	4.9 ± 0.2
	Control #2	-	0.19 ± 0.08	4.9 ± 0.2
	450	1.60	0.19 ± 0.33	5.0 ± 0.2
	450	3.20	0.20 ± 0.07	4.8 ± 0.2
	635	1.60	0.21 ± 0.07	5.1 ± 0.2
	635	3.20	0.20 ± 0.05	5.2 ± 0.1
	808	1.60	0.20 ± 0.04	5.0 ± 0.2
579.6	Control #1	-	0.21 ± 0.23	5.9 ± 1.9
	Control #2	-	0.19 ± 0.23	6.5 ± 2.6
	450	1.60	0.19 ± 0.17	5.0 ± 1.5
	450	3.20	0.20 ± 0.10	6.3 ± 1.5
	635	1.60	0.20 ± 0.31	5.5 ± 3.0
	635	3.20	0.20 ± 0.22	5.6 ± 2.0
	808	1.60	0.20 ± 0.16	5.4 ± 1.4

3.3.3. CW-TAS comparison results – global analysis

We used global analysis to fit the time constants of the data sets of Cyt c, both with and without CW light exposure. The wavelength range chosen for the analysis was 350-500 nm. At shorter wavelengths, there was low signal to noise ratio (S/N) due to weak probe strength. At longer wavelengths, low S/N was due to pump pulse leakage into the detector. After performing SVD analysis on each TAS data set, two principle components were determined as significant for obtaining global time constants. For the control data, SVD analysis yielded singular values of $S_1 = 0.9$, $S_2 = 0.4$, and $S_k \leq 0.1$ for $k \geq 3$. Figure 3.6 displays the first two principle spectra and kinetics. The principle kinetics were fit using Equation 3.1 and this resulted in the determination of two decaying exponential terms, along with a constant contribution. The time constants acquired from global analysis on the control data were 0.25 ± 0.03 ps and 5.1 ± 0.3 ps. The global time constants for control and CW data collections are displayed in Table 3.3, along with their uncertainties computed at the 90% confidence interval. The time constants extracted using the global fitting procedure on the data with full dosage CW light did not vary in a statistically significant way from the data without CW light. Hence, the relaxation and transition processes associated with these time constants (detailed in the discussion) were unaffected by full dosage CW light.

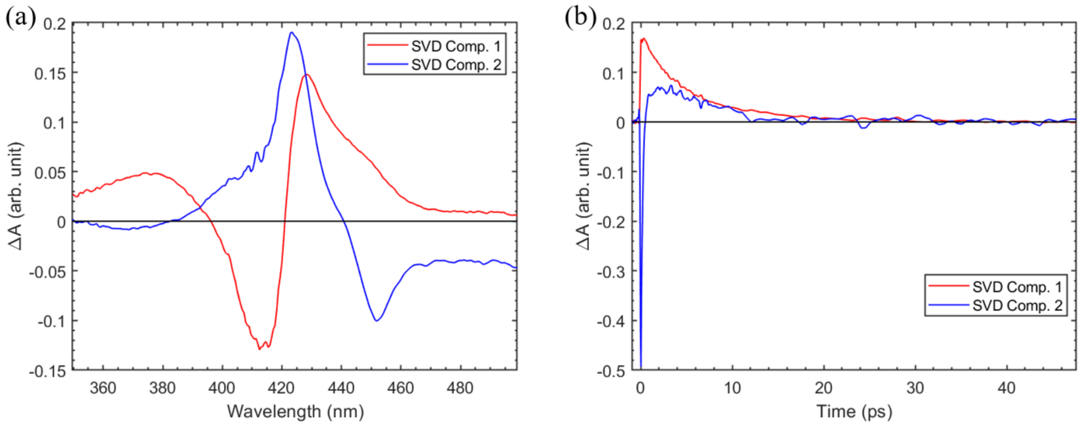

Figure 3.6 The two significant (a) spectral components and (b) kinetic components from SVD analysis on the control data of Cyt c_{red} with the wavelength range of 350-500 nm.

Table 3.3 Global analysis fitting results for reduced Cyt c. Control sets were calculated with n = 14, whereas CW data sets were calculated with n = 5, except in the case of 635-nm CW at 3.20 mW/cm^2 where n = 6.

CW Wavelength (nm)	CW Irradiance (mW/cm^2)	τ_1 (ps)	τ_2 (ps)
Control #1	-	0.25 ± 0.03	5.1 ± 0.3
Control #2	-	0.26 ± 0.03	5.1 ± 0.4
450	1.60	0.20 ± 0.11	5.3 ± 0.6
450	3.20	0.20 ± 0.05	5.0 ± 0.5
635	1.60	0.25 ± 0.06	5.1 ± 0.5
635	3.20	0.26 ± 0.03	5.0 ± 0.3
808	1.60	0.26 ± 0.05	4.9 ± 0.4

3.4. Discussion

3.4.1. Kinetic and global analyses

In our study, kinetic and global analyses of Cyt c yielded similar results, producing two time constants. We took both a kinetic and global analysis approach to analyzing TAS data of Cyt c, both without and with concurrent low-level CW light. Although more commonly used in pump-probe spectroscopies with a single wavelength probe pulse, kinetic analysis techniques can also be used to provide a first glimpse at the kinetic processes prior to global analysis. For broadband probe pulses, global analysis techniques are widely considered the standard approach for data analysis [98,99]. The longer time constant (5.1 ± 0.3 ps) is consistent with previous TAS studies on Cyt c using 532 nm excitation [93]. The authors concluded this time constant corresponds to recombination of the distal methionine (Met-80) to the porphyrin Fe in the Cyt c active site. The shorter time constant (0.25 ± 0.03 ps) is consistent with the shorter relaxation values attributed to vibrational relaxation of the heme [92,93].

A time constant in the range of 2.5-2.8 ps was reported in previous studies [92,93], however, when the number of time constants used in our global analysis was increased, our SVD analysis did not resolve an approximately 2.5-ps time constant. In Wang *et al.*, the relative contribution of the 2.8-ps time constant is consistently weaker than the contributions from other time constants [92]. Additionally, in Negrerie *et al.*, the first SVD component is predominantly composed of the 4.8-ps time constant, and dwarfs the contribution from the 2.5-ps time constant [93]. Given that the noise level in our data at certain wavelengths is not optimal, as shown in Figure 3.5, it is likely that the 2.5-ps time constant could not be resolved due to the noise in the data. Therefore, to determine if the 2.5-ps time constant is resolvable in our samples, more replicates are needed to increase the signal-to-noise ratio (S/N). A longer (16 ps) time constant was also resolved by Negrerie *et al*. [93]. Their study notes that the 16-ps time constant had a minor contribution compared to the 4.8-ps time constant, and their extended time window (out to 100 ps of time delay) helped them to further resolve the 16-ps time constant. Our analysis likely did not resolve the 16-ps time constant because the 16 ps time constant is a weaker contribution which requires higher S/N to resolve.

3.4.2. Effect of CW exposures on Cyt c TAS

In this study, both TAS and CW-TAS studies were performed on the reduced form of Cyt c. The choice of CW wavelength and dosimetry were meant to approximate exposures expected to generate PBM-like effects, based on results from previous studies [64,101]. In this way, we expected to identify whether Cyt c alone could account for the initial photon absorption and electronic state dynamics of PBM. We found that for low-level CW exposures at 450 nm, 635 nm, and 808 nm we could not distinguish any new transients (ΔA) beyond the noise floor in the TAS data. Additionally, we found no significant differences in the time constants for any transient signals due to CW illumination (Table 3.3). It is likely that the reason that there are no measurable changes with the CW exposures is that the ground state absorption for Cyt c is weak at the wavelengths selected for the CW exposures. This leads us to eliminate Cyt c as a primary target of PBM with a mechanism of electronic transition. Alternatively, our results are consistent with a mechanism for PBM that does not require electronic excited states.

One limitation to our study was that we only probed the Soret region by using the 532-nm pump. Although we only did one control experiment to look at the Q band of Cyt c (Fig. A.2), it is highly unlikely that probing within the Q band would have changed the outcome because any electronic change should affect *both* the Q and Soret regions [86].

Although we did not see an effect of CW light on the excited state dynamics of Cyt c, we did show that it is possible to successfully incorporate low-irradiance CW light into the Helios system without altering the TAS data. As presented in Tables 3.2 and 3.3, there were no statistically significant differences in electronic state dynamics between our data sets with and without CW exposures as determined by both kinetic and global analyses. Finally, we have established the combined CW-TAS method as a viable method for screening proteins, or enzyme complexes, for potential involvement in the electronic initiation of PBM by careful choice of CW wavelength and dosimetry.

3.5. Conclusion

We have presented a modified method of TAS to include the introduction of steady-state CW laser exposure in real time with repeated TAS measurements. The CW irradiation did not alter the results of the TAS measurements using the reduced form of Cyt c. When using CW wavelengths and dosimetry reasonably expected to induce NO in cells, and potentially lead to PBM in animal systems, we were unable to identify electronic transients above background levels for Cyt c protein, likely due to the weak absorbance at the CW wavelengths utilized in our study. We hypothesize that electronic transitions will be induced for protein targets which do have strong absorbance at the selected CW wavelength and these targets will be candidates for involvement in the initial step in the

PBM process. To underpin our results with CW exposure, our kinetic and global analyses produced data consistent with that previously published. The CW-TAS method will provide a means for assessing other mitochondrial proteins and enzyme complexes for a role in PBM initiation via electronic transition.

4. MAMMALIAN COMPLEX III HEME DYNAMICS STUDIED WITH PUMP-PROBE SPECTROSCOPY AND RED LIGHT ILLUMINATIONS[*]

4.1. Introduction

Photobiomodulation (PBM) is the use of low irradiance light in the red to near-infrared (NIR) wavelength range to generate beneficial biological effects in living cells and tissues. Mitochondria, which are the primary organelles involved with ATP production for eukaryotic organisms, are generally accepted as the key targets of PBM therapy [77]. The leading hypothesis for the origin of the PBM effect within the cell is that light modulates the properties associated with the enzyme complexes within the electron transport chain (ETC). Notably, complex IV (C-IV) of the ETC has been a protein of interest among PBM researchers due to the overlap of its absorption spectrum with that of the action spectrum of PBM [78–83].

For the purposes of this study, relatively high concentrations of protein are necessary, and unfortunately C-IV was not available commercially at a concentration higher than 5 mg/mL. In contrast, C-III was commercially available as a lyophilized powder, allowing us to easily make high concentration solutions. Recent work from our group has suggested C-III activity may be altered by low-intensity NIR exposures [102].

---

[*] Reprinted with permission from "Mammalian complex III heme dynamics studied with pump-probe spectroscopy and red light illuminations" by S. P. O'Connor, S. M. Powell, J. M. Rickman, N. J. Pope, G. D. Noojin, M. O. Scully, M. L. Denton, and V. V. Yakovlev, 2021, Biomed. Opt. Express, **12**(11), 7082-7091, Copyright 2021 by Optica Publishing Group. (Reference [124])

While it remains unclear if this is a direct effect on C-III, or is due to indirect effects on C-IV, this makes C-III an appealing target for further study.

C-III has been recently studied with the transient absorption spectroscopy (TAS) technique [90,91]. TAS is a pump-probe spectroscopic technique that can characterize the photophysical dynamics of biological and chemical systems [18]. Though the electronic transitions of C-III have previously been studied via TAS, this work was conducted on proteins from yeast (*Saccharomyces cerevisiae*) [90] and photosynthetic bacteria (*Rhodobacter capsulatus*) [91]. TAS characterization of C-III from a mammalian source, such as porcine or bovine, has not been previously conducted. Porcine C-III is highly similar to human C-III (89.54% identity, vs 55.38% and 40.31% identity for the yeast and bacterial C-III respectively) and will be more likely to be predictive of human C-III electronic transitions/time constants, and thus more relevant to human PBM exposures. Therefore, in this study, we focused our efforts on the TAS characterization of C-III from a mammalian source.

Recently, we developed a new technique combining continuous wave (CW) light with TAS, called CW-TAS, for testing samples with light exposures consistent with those found to induce PBM effects [103]. The proof of principle for this technique was established through testing cytochrome c, the heme protein responsible for mediating the electron transfer from C-III to C-IV. No PBM effects were expected when testing with cytochrome c, and indeed the TAS data remained intact and unchanged with the addition of the CW exposures. To further test the CW-TAS technique and to probe potential PBM effects, the more complicated ETC protein, C-III, was tested in this study to investigate if exposures consistent with PBM alter the TAS profile of C-III.

In the present study, we investigate porcine C-III with TAS and characterize the time constants for the oxidized and c_1 reduced redox states. This provides the first TAS characterization of C-III specifically from a mammalian source, and we compare the results to previous studies of yeast and bacterial C-III [90,91]. Additionally, we investigate the response of mammalian C-III to irradiances from a CW light source at 635 nm using our previously developed CW-TAS methodology [103]. Since PBM greatly affects mitochondria and its functions [77] and heme proteins are a central part of oxidative phosphorylation, we hypothesize that PBM like changes to C-III will manifest as changes to its transient absorption response, such as production of new transient signals, quenching of existing signals, or changes in the time constants. We prepare C-III in its partially reduced redox state and test it both with and without red CW light exposures during the TAS measurement. By comparing the CW irradiated TAS data to the control, the measured heme dynamics of C-III can be implicated or eliminated as a mechanism underlying the initiation of PBM, leading to a better understanding of the origin of the effect.

4.2. Methods

4.2.1. Sample preparation

Complex III from porcine heart was purchased from Sigma-Aldrich (C3381). Complex III (12.5 mg/mL) was prepared in 20 mM $KHCO_3$ (237205, Sigma-Aldrich), pH 8.0 with 20 mM n-dodecyl-β-D-maltoside non-ionic detergent (DDM) (D4641, Sigma-

Aldrich). To produce reduced samples of complex III, the sample was prepared in a cuvette sealed with a septum screwcap with a rubber stopper. The sample was purged using gaseous N_2 for five minutes. A syringe was then inserted to inject a solution of sodium dithionite (157953, Sigma-Aldrich) to reduce the sample. This reduced form of C-III is referred to in this study as sodium dithionite-treated C-III (SDT-C-III). The oxidation state of all samples was verified by UV-VIS spectroscopy using a Cary 6000i spectrophotometer prior to all TAS experiments. Samples were assayed in a quartz cuvette with a 2-mm path length.

4.2.2. Transient absorption spectrometer setup

All TAS experiments were carried out using the HELIOS Fire (Ultrafast systems) transient absorption spectrometer described in our previous study [103] (See section 3.2.2). The pump and probe sources were provided by a Ti:sapphire regenerative amplifier (SpitFire Ace, Spectra-Physics) with wavelength centered at 800 nm, pulse duration of 80 fs, and repetition rate of 1 kHz. The pump pulses were generated by splitting part of the 800 nm source light to an optical parametric amplifier (OPA; TOPAS-Twins, Light Conversion), where it was converted to 418 nm light (FWHM ~8 nm) by the method discussed in previous studies [54,55]. The pump light traveled through a chopper wheel to reduce the repetition rate to 500 Hz. The beam radius of the pump pulse was determined to be about 100 μm at its focal point using the knife-edge technique [96] assuming a $1/e^2$ beam waist. The probe pulse consisted of a supercontinuum (430-760 nm) generated from the fundamental 800-nm pulse incident upon a sapphire window, also having a repetition rate of 1 kHz. Figure 4.1 displays a typical supercontinuum generated for the probe pulse.

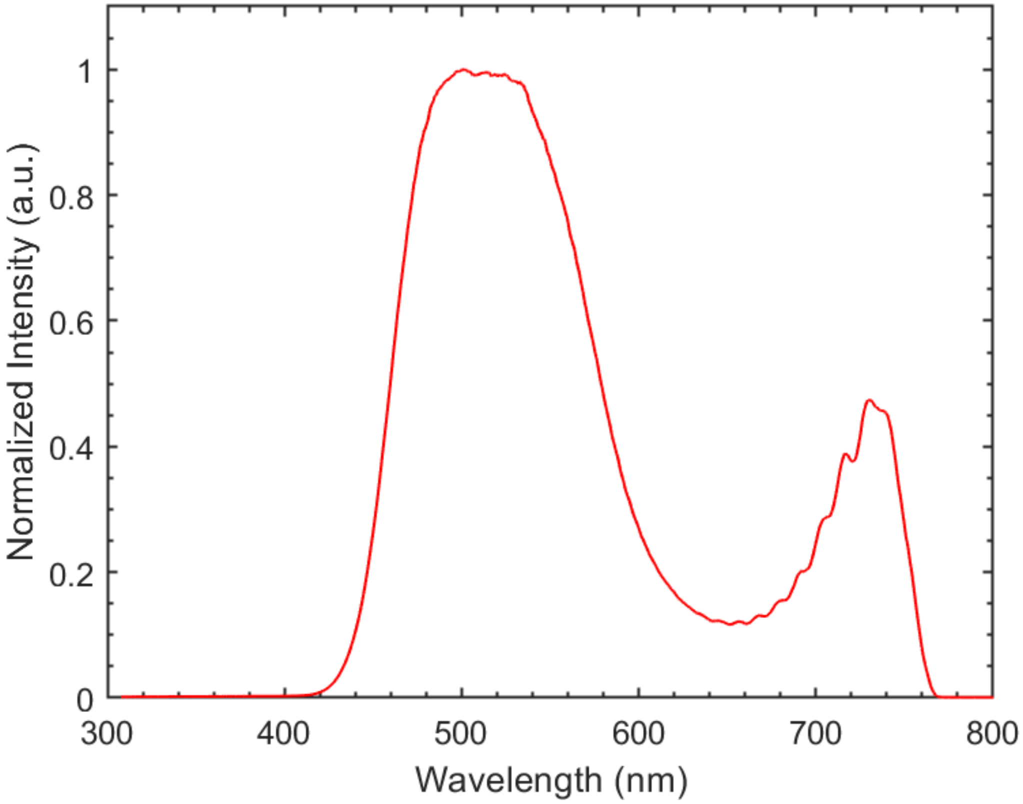

Figure 4.1 Supercontinuum spectra generated from the sapphire window.

4.2.3. Low-irradiance CW laser diode setup

Output from a 635 nm laser diode (CPS635, Thorlabs) was coupled into a fiber imaging system to provide low-power CW irradiation to the sample during TAS scanning. The output power of the diodes was controlled with a continuously variable neutral density filter (NDL-25C-2, Thorlabs) prior to coupling into the 550-µm diameter fiber (M37L02, Thorlabs). The fiber output was imaged to the sample with a flat top beam profile having a diameter of 0.95 cm, resulting in an area of 0.71 cm^2 at the cuvette. As detailed previously [103], the fiber output was placed above the pump-probe beam plane, and directed to the cuvette at a shallow angle so that the diode light was not collected at the collection fiber of the HELIOS Fire. The light from the laser diode illuminations did not affect the ΔA(λ, t) spectrum, as verified through observation of the real time ΔA(λ) spectrum in the HELIOS software.

4.2.4. Testing parameters

For the TAS procedure, the 418 nm pump wavelength was used with a power of 100 μW, and the VIS supercontinuum was used for the probe pulse. The pump and probe pulse overlap was optimized before the start of each TAS measurement by testing with a solution of tetrakis(4-sulfonatophenyl)porphyrin, which is responsive to TAS at our pump wavelength [104], and maximizing the signal response using the Helios spectrometer. For the oxidized C-III, the time delay setup for each scan was programmed to take 0.2-ps steps from -2 to 0 ps, 0.05-ps steps from 0 to 6 ps, 0.2-ps steps from 6 to 25 ps, 1.0-ps steps from 25 to 100 ps, and 25-ps steps from 100 to 7500 ps for a total of 401 time steps. At each time delay step, 0.5 s of measurement were taken, which resulted in 250 ΔA(λ, t) measurements averaged together at that time delay. TAS tests of oxidized C-III were performed without the 635 nm CW exposures, whereas SDT-C-III were performed both with and without the CW exposures.

For the SDT-C-III, the time delay setup for each scan was programmed to take 0.2-ps steps from -2 to 0 ps, 0.05-ps steps from 0 to 3 ps, 0.1-ps steps from 3 to 10 ps, 0.5-ps steps from 10 to 100 ps, and 5-ps steps from 100 to 500 ps for a total of 401 time steps. Similar to the oxidized sample, 0.5 s of measurement were also taken at each time delay step for SDT-C-III. The TAS program was set to take a total of 9 contiguous time scans for each replicate of SDT-C-III tested. For the collections that involved red light irradiances, the first scan was taken as a baseline and did not have any CW laser diode light incident upon the sample. Scans 2-6 were taken with the CW diode emitting light onto the C-III sample with a power density of 4.7 mW/cm^2 at the cuvette. Scans 7-9 were taken with the CW diode turned off to observe changes after the full dosage of irradiation [64]. The total time to record 9 scans was 55 min and 47 ± 5 s. The duration of the CW diode exposure during scans 2-6 was computed to be 30 min and 59 ± 3 s. This resulted in an energy density of 8.74 ± 0.02 J/cm^2 at the cuvette over scans 2-6. Five replicate data collections were performed with CW-TAS and the red CW laser diode.

4.2.5. Data processing and analysis

Data was collected and exported from the Helios FIRE software and processed in Surface Xplorer (version 4.3.0, Ultrafast Systems). Background subtractions were performed using the spectra taken at the time delays prior to time-zero. Chirp correction was performed for each data set, and the time-zero correction was acquired by fitting the coherence spiking near the zero delay time in the surface data. CW data sets were processed by averaging together each scan from a replicate sample to the same scan number from other replicate data collections. For data sets without CW exposure, each of the scans within the data collection were averaged together. Global analysis techniques were used to acquire time constants of the excited state dynamics.

Global analysis was conducted in Surface Xplorer by first performing principle component analysis on the surface data through singular value decomposition (SVD) as detailed in previous studies [99]. Time constants were then acquired by fitting the principal components with a sum of exponential decays convolved with a Gaussian instrumentation response function [98], displayed in Equation 4.1.

$$C(t) = \exp\left[-\left(\frac{t-t_0}{t_p}\right)^2\right] * \sum_i A_i \exp\left[-\frac{t-t_0}{\tau_i}\right] + A_0 \quad , \quad t_p = \frac{w_{FWHM}}{2\ln(2)} \qquad (4.1)$$

Equation 4.1 displays the kinetic model, C(t), as a function of time (t) between the pump and probe pulses, where $*$ indicates convolution. In the equation, A_i is the magnitude contribution of each exponential decay of time constant (τ_i), t_0 is time-zero, A_0 is an optional constant offset, and t_p is a fit parameter relating to the Gaussian IRF's full width at half maximum (FWHM) shown as w_{FWHM}.

4.3. Results and Discussion

4.3.1. Absorption spectra of mammalian complex III

Figure 4.2 presents the ground state absorbance spectra of both oxidized and SDT-C-III. Oxidized C-III had a strong absorption peak in the Soret band at 407 nm. The Soret peak for SDT-C-III was red-shifted with a λ_{max} at 425 nm, and in the Q band, there were peaks at 521 nm and 551 nm. The 418-nm pump's bandwidth (FWHM ~8 nm) overlapped with the Soret absorption peaks of both dithionite-treated and oxidized C-III and allows for the excitation of both species.

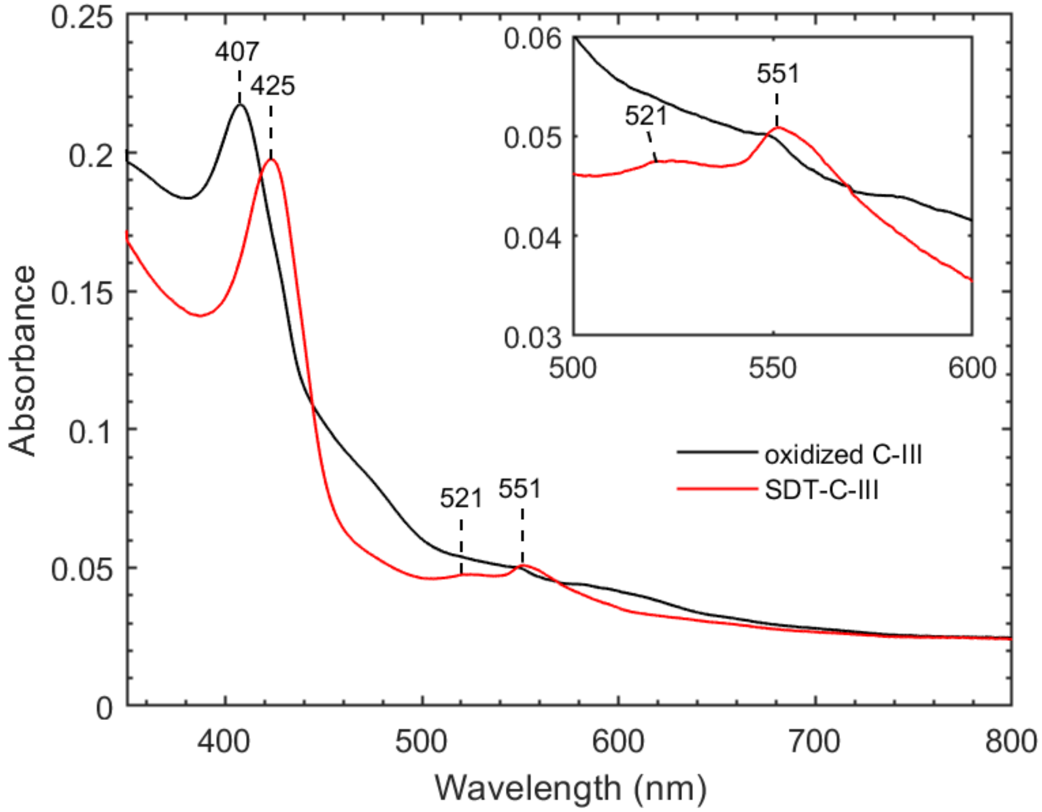

Figure 4.2 Ground state absorbance spectra for C-III measured in its initial oxidized state (black) and after sodium dithionite-treatment (red). Inset plot displays a magnified view of the Q bands.

For the SDT-C-III in this study, the absorbance peaks at 521 nm and 551 nm were indicative of a full reduction of the c_1 hemes in the proteins [105]. However, our spectra did not display a second pair of sharp absorbance peaks at ~530 nm and ~560 nm, which would be an indicator for the full reduction of the b hemes. When further reduction of the sample was attempted with higher concentrations of sodium dithionite, the proteins formed visible aggregates with no further features in the spectra. However, the 551 nm peak did display a shoulder on its right-hand side which would indicate a partial reduction of the b hemes. This partial, and not full, reduction of the b hemes is quite possibly due to the relatively high concentration of C-III used in this study, and this has similarly been noted in the previous C-III study by Chauvet *et al.* [90]. We conclude that our dithionite-treated C-III is in a partially reduced state with fully reduced c_1 hemes and a partial reduction of the b hemes.

4.3.2. TAS results of C-III

Transient absorption surface data was collected for samples of oxidized C-III and SDT-C-III and displayed in Figures 4.3(a) and 4.4(a), respectively. For global analysis, the surface data was constrained to the time delay range of -1 to 50 ps and wavelength range of 455-750 nm. The shortened time range was selected to focus on the shorter transients associated with the heme dynamics as opposed to the long-lived transient response. The wavelength range was selected to avoid the pump pulse leakage at shorter wavelengths and the weak probe strength at higher wavelengths. SVD analysis for oxidized C-III yielded singular values of $S_1 = 0.34$, $S_2 = 0.15$, and $S_k \leq 0.07$ for $k \geq 3$, and the first two spectral (Fig. 4.3(c)) and kinetic (Fig. 4.3(d)) components were thus found to be significant and used for global analysis. For SDT-C-III, the singular values were found to be $S_1 = 0.26$ and $S_k \leq 0.04$ for $k \geq 2$, and the first spectral (Fig. 4.4(c)) and kinetic (Fig. 4.4(d)) component was found to be significant and used for global analysis. The principal kinetics were fit using Equation 4.1 and for oxidized C-III yielded global time constants of $t_1 = 0.12 \pm 0.03$ and $t_2 = 3.3 \pm 0.3$ while for SDT-C-III yielded values of $t_1 = 0.09 \pm 0.05$, $t_2 = 0.6 \pm 0.1$, and $t_3 = 4.9 \pm 0.4$. The uncertainty for these values come from the 90% confidence interval of the fit.

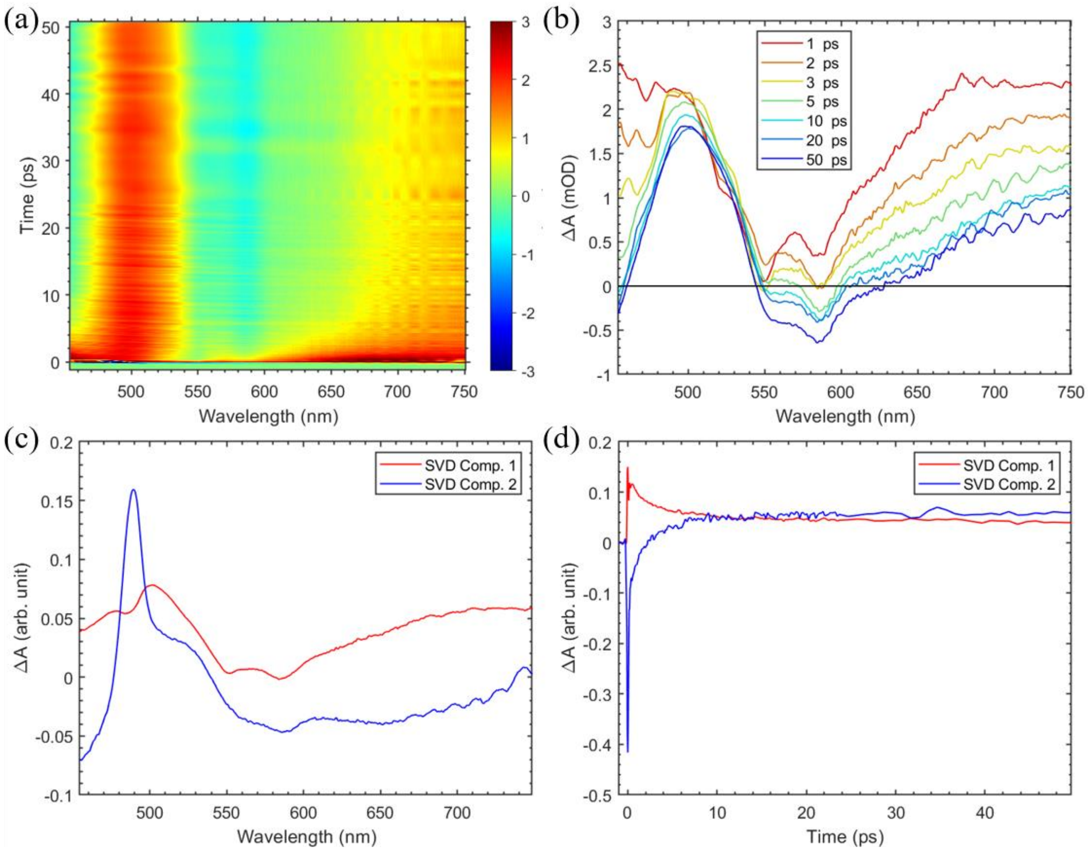

Figure 4.3 Transient absorption spectra of oxidized C-III with 418 nm excitation at 200 nJ/pulse displayed as (a) a surface and (b) spectral cross sections at the constrained time-delay range used for global analysis. Also provided are the first two (c) spectral components and (d) kinetic components from SVD analysis.

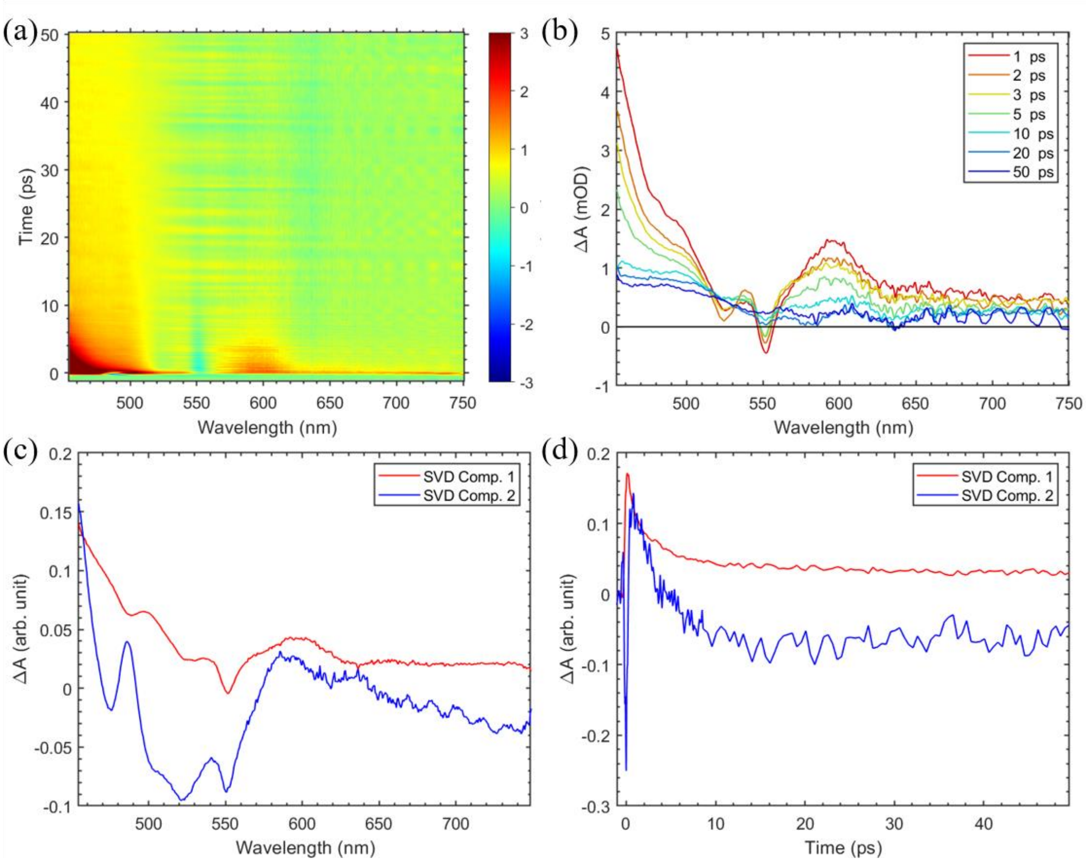

Figure 4.4 Transient absorption spectra of SDT-C-III with 418 nm excitation at 200 nJ/pulse displayed as (a) a surface and (b) spectral cross sections at the constrained time-delay range used for global analysis. Also provided are the first two (c) spectral components and (d) kinetic components from SVD analysis.

The global time constants for the ~3-7 ps heme dynamics (τ_{Heme}) of C-III are tabulated in Table 4.1, along with the previously reported values from earlier studies. The time constants at this timescale, for the reduced states, have been documented to be the recombination time following axial ligand photodissociation [90,91]. For the oxidized state, time constants at this scale have been previously attributed to vibrational cooling [91,93,106]. The τ_{Heme} associated with this study's porcine SDT-C-III is listed to be in the c_1 reduced state following the conclusion drawn from its ground state absorption spectra. The SDT-C-III τ_{Heme} value obtained from our analysis was close to the τ_{Heme} value that was reported for the bacterial C-III and a little faster than the τ_{Heme} value reported for the yeast C-III with similar redox states. The oxidized C-III τ_{Heme} value was also similar to the value reported in the bacterial C-III study.

Table 4.1 Global time constant values associated with the heme dynamics (~5-7 ps) measured in TAS studies on different redox states of C-III.

Study	Source	Excitation (nm)	Redox state	τ_{Heme} (ps)
This work	Porcine	418	c_1 reduced [a]	4.9 ± 0.4
	Porcine	418	oxidized [a]	3.3 ± 0.3
Vos et al. [91]	Bacterial	570	bc_1 fully reduced	6.2
	Bacterial	520	bc_1 fully reduced	6.0
	Bacterial	520	c_1 reduced	4.8
	Bacterial	520	oxidized	3.1
Chauvet et al. [90]	Yeast	523	c_1 reduced	5.4
	Yeast	523	b reduced [b]	6.8

[a] Analysis was performed with n = 6 scans averaged together for the c_1 reduced state and n = 8 scans for the oxidized state. Uncertainty was computed at the 90% confidence interval of the fit.

[b] Authors estimate that 70% of b hemes were reduced in their preparation.

4.3.3. CW-TAS results of C-III with 635 nm light

Following the characterization of oxidized C-III and SDT-C-III with the standard TAS procedure, the CW-TAS procedure was performed on n = 5 replicate samples of SDT-C-III. The choice of dosimetry and the 635 nm CW wavelength were meant to approximate exposures expected to generate PBM-like effects, based on results from previous studies [64]. Following data collection and pre-processing, SVD was performed on each of the nine scans of the TAS data taken on SDT-C-III. The wavelength range chosen for global analysis was 455-750 nm. The time delay range was selected to be -1 to 50 ps to focus on the transient responses of 3-7 ps, corresponding to the heme dynamics which were characterized previously with TAS. SVD analysis performed on the CW-TAS data yielded singular values for each scan number of $S_1 \geq 0.22$ (to a maximum of 0.30), $S_2 = 0.05$, and $S_k \leq 0.03$ for $k \geq 3$. The first component of the principal kinetics and spectra were thus determined to be the most significant and used for comparative analysis among scan numbers.

Global time constants were computed using the first principal kinetic component of each scan from the CW irradiated collection, and the time constants τ_{Heme} corresponding to the ~5-7 ps heme dynamics are tabulated in Table 4.2. The τ_{Heme} time constant was found to be within the range of 4.7-5.2 ps throughout each of the nine scans. Since the time constants did not deviate outside of the overlap of the confidence intervals, we conclude that the time constant did not change significantly. Because the τ_{Heme} time constant remained near the previously obtained SDT-C-III value of 4.9 ± 0.4 ps, and did not approach the oxidized C-III value 3.3 ± 0.3 ps, we conclude that the sample remained in the c_1 heme reduced state throughout the CW-TAS procedure. Moreover, the b hemes were not reduced further in any significant way because the time constants did not shift to 6-7 ps based on the values from previous studies [90,91] (see Table 4.1). Consequentially, this implies that the c_1 heme's ligand photodissociation and recombination process remained to be the dominant process observed throughout the CW-TAS procedure, and the CW light did not induce a significant shift towards vibrational cooling associated with the oxidized state or towards the ligand photodissociation and recombination associated with the b hemes.

Table 4.2 Global time constants associated with the heme dynamics (~5-7 ps) for SDT-C-III during the CW-TAS collection with the red CW diode light. Scans were averaged from n = 5 replicate tests, and uncertainty was computed at the 90% confidence interval of the fit.

Scan #	CW light	τ_{Heme} (ps)
1	Off	4.9 ± 0.4
2	On	4.9 ± 0.4
3	On	4.9 ± 0.4
4	On	5.1 ± 0.5
5	On	5.1 ± 0.5
6	On	5.2 ± 0.6
7	Off	4.7 ± 0.4
8	Off	4.7 ± 0.4
9	Off	5.2 ± 0.5

The first principal spectral component from each of the nine contiguous TAS surfaces are displayed in Figure 4.5. For both the control (Fig. 4.5(a)) and CW-irradiated (Fig. 4.5(b)), the spectral components did not develop new peaks that would indicate a sharp change in redox state. Relative magnitude changes with progressing scan number were noted among both collections, such as the relaxation of the minima located ~487 nm and the relaxation at the wavelength range 520-580 nm. Because both the control and CW irradiated data contained these changes, we conclude that the magnitude shifts in the spectra were not the result of a CW induced PBM effect within SDT-C-III and were a naturally occurring change in the samples over time. Comparing with previously obtained first principal spectra from oxidized C-III (Fig. 4.3(c)) and SDT-C-III (Fig. 4.4(c)), we correlate the relaxation as a slight shifting of the SDT-C-III spectra towards the oxidized state. Based on these observations, we further conclude that the shifts in magnitude in both the control and CW irradiated data were a result of a slight oxidation of the samples over time. Since the 635 nm CW light is below the energy of the Q-band absorbance peaks for the reduced states of C-III, this selection of CW wavelength was likely too low of energy to stimulate measurable PBM-like effects in our study. Future experiments with C-III should consider a CW wavelength selected from a 520-560 nm range to overlap with an absorbance peak from the reduced c_1 or b hemes.

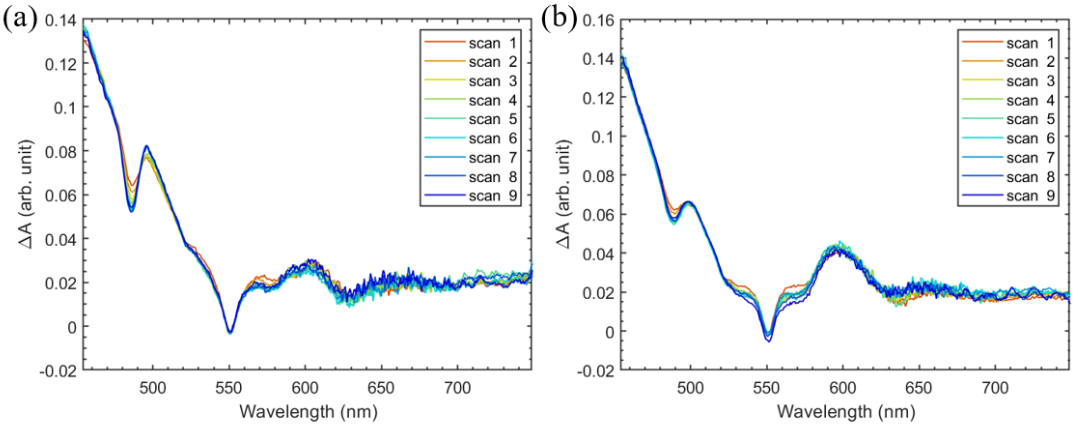

Figure 4.5 First principal spectral components from SVD analysis on each of the nine TAS surfaces for the (a) control and (b) CW irradiance collections on SDT-C-III.

4.4. Conclusion

We have presented the first TAS characterization on C-III specifically from a mammalian source. For porcine C-III, the time constants were found to be 3.3 ± 0.3 ps for vibrational cooling of the oxidized state and 4.9 ± 0.4 ps for rebinding of the photodissociated axial ligand of the c_1 reduced state. These time constants are in agreement with previous results obtained on bacterial C-III by Vos *et al.* [91]. We found that CW-TAS measurements with 635 nm light on SDT-C-III did not induce a change in the time constant τ_{Heme}, which implied that the sample remained almost entirely in the c_1 reduced state. Based on further analysis of the principal spectra, both with and without CW light, SDT-C-III had undergone a slight oxidation over time in both the control and CW samples. Thus, the slight oxidation was not directly a result of CW light stimulation of the sample. We rule out the possibility of 635 nm CW light at 4.7 mW/cm^2 inducing a PBM effect on C-III, specifically with the photodissociation of the axial ligand. The elimination of this electronic process contributes towards a better understanding of PBM by narrowing down the possible electronic or molecular transitions that could be implicated to initiate the PBM effect.

5. SPECTRAL RESOLUTION ENHANCEMENT FOR IMPULSIVE STIMULATED BRILLOUIN SPECTROSCOPY BY EXPANDING PUMP BEAM GEOMETRY

5.1. Introduction

Brillouin spectroscopy has emerged as a powerful tool to non-invasively assess variations in viscoelastic properties in cells and tissues [107–110]. Many Brillouin spectroscopy and microscopy systems utilize the spontaneous Brillouin scattering effect [111–113]. Spontaneous Brillouin scattering refers to light which scatters from acoustic phonons generated in the medium which were induced by thermal or quantum-mechanical zero-point effects [4]. On the other hand, light scattering from acoustic phonons which are induced by an applied electric field results in stimulated Brillouin scattering (SBS). SBS microscopy was introduced to increase the speed of imaging and to improve spatial resolution in imaging applications [114,115]. SBS microscopy does have a limitation of continuous scanning of one of the excitation wavelengths which requires time for each acquisition. However, this limitation is circumvented with impulsive stimulated Brillouin scattering (ISBS) which makes use of the transient grating spectroscopy technique [20]. ISBS spectroscopy takes advantage of time-resolved measurements and allows spectral measurements to be done in the time-domain for greater stability and reproducibility which are often difficult to achieve in spontaneous Brillouin microscopy measurements [116].

Within recent years, ISBS has been introduced to biomedical applications [23–25,117,118]. This began when the technique was first applied to flow cytometry studies

[117], which demonstrated its capability for measuring vascular-like environments. Following this, the concept of ISBS microscopy was introduced with the first ISBS images [23]. In this study, ISBS was demonstrated to distinguish between different liquids in a partitioned cell as well as image liquids in a narrow spatial geometry in a microfluidic device. Shortly thereafter, ISBS microscopy was demonstrated to distinguish between hydrogels of differing stiffness and the spatial resolution was improved [24].

Towards the development of ISBS microscopy, it is important to consider both the spatial and spectral resolution of the system [119]. The spatial resolution for the ISBS technique has been improved in recent research where the lateral resolution has approached the cellular scale [24]. However, the effects of instrumentation on ISBS linewidth in the Fourier domain and improvements to spectral resolution have not been previously explored, to the best of our knowledge. The choice of instrumentation has been previously shown to cause spectral broadening in the case of spontaneous Brillouin imaging [120], which can impact the spectral resolution of the instrument. High spectral resolution is essential for Brillouin techniques for resolving subtle changes in the Brillouin spectra and for distinguishing between two close elastic responses. Here, we aim to provide a first look into improving spectral resolution towards ISBS microscopy.

In this report, we studied the influence of the initial pump beam geometry on the frequency and linewidth of the ISBS signal. The linewidth of the frequency-domain ISBS signal was found to be dependent on the initial pump beam diameter. By expanding the pump beam and focusing it with a cylindrical lens, the spectral resolution in ISBS measurements can be increased allowing for a higher resolvability of two close elastic responses. This paper first presents our ISBS experimental setup along with the sample preparation, data processing methodologies, and pump beam variation procedure. We first show the effects of spike artifact removal on the ISBS signal symmetry, and we present and evaluate our curve-fitting methodology for closely fitting the ISBS signal profile. Then, we present the effects of magnifying the pump beam diameter on the ISBS signal in the time and frequency domains, and we evaluate the effect on the ISBS frequency and linewidth.

5.2. Methods

5.2.1. ISBS setup

ISBS measurements were taken with our experimental setup displayed in Figure 5.1. Pump pulses were provided by a pulsed fiber laser (wavelength: 532 nm, 1-ns pulse duration, GLPR-10, IPG Photonics) which was operated at a 20 kHz repetition rate. A fraction of the pump pulse power was split off using the polarizing beam splitter (PBS, Fig. 5.1) towards the photodiode (DET10A, Thorlabs; PD, Fig. 5.1) to act as an oscilloscope trigger for signal collection. The probe laser was provided by a CW diode laser (wavelength: 780 nm, TEC 520, Sacher Lasertechnik) which provided an output power of 12 mW. The probe beam was collimated and expanded using a 4f setup upon leaving the laser module (f_3/f_4, Fig. 5.1).

The pump pulses were focused in the y-direction using a 200-mm cylindrical focusing lens (CL, Fig. 5.1), and the probe laser was focused with a 200-mm spherical focusing lens. The two beams were combined collinearly using a long-pass dichroic mirror (DM, Fig. 5.1) and propagated towards the transmission grating (48 μm grating period;

TG, Fig. 5.1) such that both beams focused onto the grating. The ±1st order modes of both the pump and probe light were re-imaged with the 4f telescope setup (f_5/f_6, Fig. 5.1) into the sample site (S, Fig. 5.1), and ISBS was thus conducted in the heterodyne configuration [121]. Higher order modes (±2, ±3, etc.) along with the 0th order mode were blocked at the Fourier plane of the 4f setup.

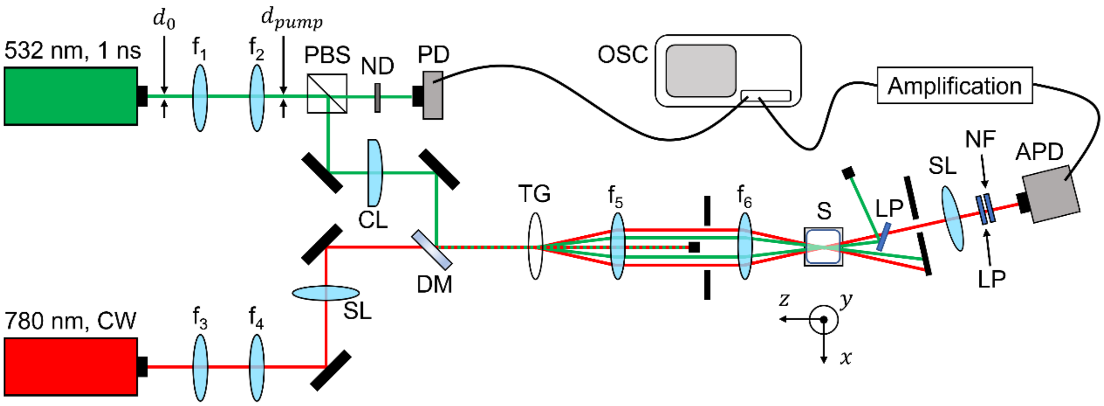

Figure 5.1 Schematic of the ISBS experimental setup. APD – avalanche photodiode, CL – cylindrical focusing lens, DM – dichroic mirror, f_1/f_2 – pump beam expander setup, f_3/f_4 – probe beam expander setup (50mm/75mm lenses), f_5/f_6 – ISBS 4f telescope (150mm/50mm lenses), LP – long-pass filter, ND – neutral density filter, NF – 532 nm notch filter, OSC – oscilloscope, PBS – polarizing beam splitter, PD – photodiode, S – sample, SL – spherical focusing lens, TG – transmission grating.

For collection, the probe beam was focused with a spherical focusing lens into an avalanche photodiode (APD210, MenloSystems), and a long-pass filter as well as a 532 nm notch filter (NF, Fig. 5.1) were placed before the detector to remove 532 nm light. The electrical signal from the avalanche photodiode was then amplified by two low-noise amplifiers (ZFL-1000LN+, Mini-Circuits). An RF terminator was also incorporated (BTRM-50+, Mini-Circuit) to mitigate signal reflections. The electrical signal was then transferred into an oscilloscope (InfiniiVision DSOX6004A, 6 GHz bandwidth, 20 GSa/s, Keysight).

5.2.2. Sample preparation

Samples of acetone were prepared in cuvette by pipet from the original bottle with no further preparation thereafter. Bio-relevant solutions consisting of citric acid, glycine, or sucrose were prepared fresh before procedures in a stock solution of 1 M in distilled water. Diluted solutions of the bio-relevant solutions were performed in cuvette with new pipet tips, and 1:2 dilutions were performed with distilled water. Dilutions continued until a 1:64 dilution of the 1 M stock concentration (corresponding to 1.5625×10^{-2} M) was made. Replicate measurements with the bio-relevant solutions were done with newly made solutions made fresh before procedure.

5.2.3. Data collection and processing

ISBS data was collected at the maximum averaging mode of the oscilloscope which was 65,536 acquisitions. For each sample tested, 10 data collections at maximum averaging were performed. Since the repetition rate of the laser was set to 20 kHz, approximately 3.3 seconds were needed for contiguous measurements to be independent of each other. Therefore, data collections were performed with a 4 second delay between contiguous collections.

ISBS data exported from the oscilloscope was processed using a custom-built MATLAB script. Firstly, the data was processed in the time domain with a spike filtering procedure for samples with a spike artifact at $t = 0$. An average of the data before $t = 0$

was taken to find the baseline value for each set, and a neighborhood of 3 points centered at the peak of the spike artifact were taken and set to the baseline.

Data is then transformed into the frequency domain with a fast Fourier transform (FFT). For each sample, the 10 contiguous measurements were averaged together in the Fourier domain to reduce noise. The script then fits a custom fitting function $V(f)$, similar to a pseudo-Voigt profile, to the Fourier domain data using a sum of a Lorentzian, Gaussian, and constant offset displayed in Equation 5.1.

$$V(f) = \frac{a_1}{(f - a_2)^2 + a_3} + a_4 e^{-a_5 (f - a_6)^2} + a_7 \tag{5.1}$$

Here, f is frequency, a_j with $1 \leq j \leq 3$ and $4 \leq j \leq 6$ were the fitting parameters associated with the Lorentzian and Gaussian function, respectively, and a_7 is the constant offset. Contrasting from the standard pseudo-Voigt profile [122], the center frequencies of the Lorentzian and Gaussian were allowed to vary slightly to account for observed peak asymmetry. For the data taken from the pump beam expansion procedure, the ISBS frequency was taken from the maximum value of the profile fit with Equation 5.1. The full width at half maximum (FWHM) was taken from the whole profile and used as the measure of linewidth and spectral resolution.

5.2.4. Evaluation of curve-fitting model

To evaluate the closeness of fit of the custom fitting function $V(f)$, the fit was compared to a Lorentzian fit, a standard model for fitting Brillouin data, displayed in Equation 5.2.

$$L(f) = \frac{a_1}{(f - a_2)^2 + a_3} + a_4 \tag{5.2}$$

Similar to Equation 5.1, f is frequency, a_j with $1 \leq j \leq 3$ are the fitting parameters associated with the Lorentzian function, and a_4 is the constant offset. For the curve-fitting analysis, data was first fit using both models from Equations 5.1 and 5.2. The sum of squared residuals (SSR) was then computed for both models, and the closeness of fit for $V(f)$ compared to $L(f)$ was evaluated by taking a ratio of the two SSR values as shown in Equation 5.3.

$$SSR_{ratio} = \frac{SSR_{Eqn1}}{SSR_{Eqn2}} = \frac{\sum_j \left(y_j - V(f_j)\right)^2}{\sum_k \left(y_k - L(f_k)\right)^2} \tag{5.3}$$

Here, f_j are the discrete frequency data points for the Fourier data and y_j are the amplitude values at those frequency values. When $SSR_{ratio} < 1$, this implies that the SSR of the custom fit function is less than the SSR of the Lorentzian fit, and this implies that the custom fit would fit the data closer than the Lorentzian fit. The reverse is true when $SSR_{ratio} > 1$, and $SSR_{ratio} = 1$ indicates that the test by this metric was inconclusive.

5.2.5. Pump beam expansion and procedure

Changes to the pump beam diameter were made with two lenses in the 4f telescope setup indicated by f_1 and f_2 in Figure 5.1. This 4f telescope was constructed with optical cage equipment, and the lenses were placed in XY translation mounts in the cage. The initial pump beam diameter leaving the laser (d_0) was magnified by this telescope to the new beam diameter (d_{pump}) using the lens configurations presented in Table 5.1.

To ensure that the pump beam remained aligned after placing the lenses, the following procedure was performed for each configuration. Before placing the lenses, a collared temporary mirror was placed before the cylindrical lens directing the beam outside the experimental setup towards a second mirror external to the setup. This formed a new beam path which was twice the length of the ISBS setup itself. The beam was first aligned to the beam path using the temporary mirror and external mirror. The lenses were then placed in the f_1/f_2 telescope, and the translation knobs of the XY mounts were used to realign the beam to the external beam path. The temporary mirror was then removed allowing the beam to propagate through the ISBS system.

Table 5.1 Lenses used for each configuration and the corresponding pump diameter magnification. Positive and negative values correspond to converging and diverging lenses, respectively.

Configuration	Lens 1 (mm)	Lens 2 (mm)	d_{pump}/d_0
1	-50	75	3/2
2	none	none	1
3	75	-50	2/3
4	100	-50	1/2
5	150	-50	1/3

5.3. Results

5.3.1. Spike artifact filtering and FFT profile symmetry

For most samples tested with our system, we observed an artifact in the form of a spike at $t = 0$ in the time domain before the acoustic response began. Figure 5.2(a) displays an example of the time domain ISBS signal with the spike artifact at $t = 0$ before and after the spike removal procedure in data processing. The effect the spike has on the peak profile in the frequency domain following Fourier transformation is displayed in

Figure 5.2(b) where the FFTs of the two signals are shown. Prior to spike filtering, the peak profile typically displays an asymmetry in the form of a raised tail on the left or right side, and Figure 5.2(b) depicts an example of the tail artifact appearing on the left side. Following spike filtering, the symmetry of the peak profile significantly improved as shown in Figure 5.2(b). This peak was found for all samples of bio-relevant solutions and distilled water that were tested. We note that the spike was not appreciable in the time domain signal for samples of acetone, and we attribute this to the high magnitude of its acoustic signal overcoming the magnitude of the spike artifact.

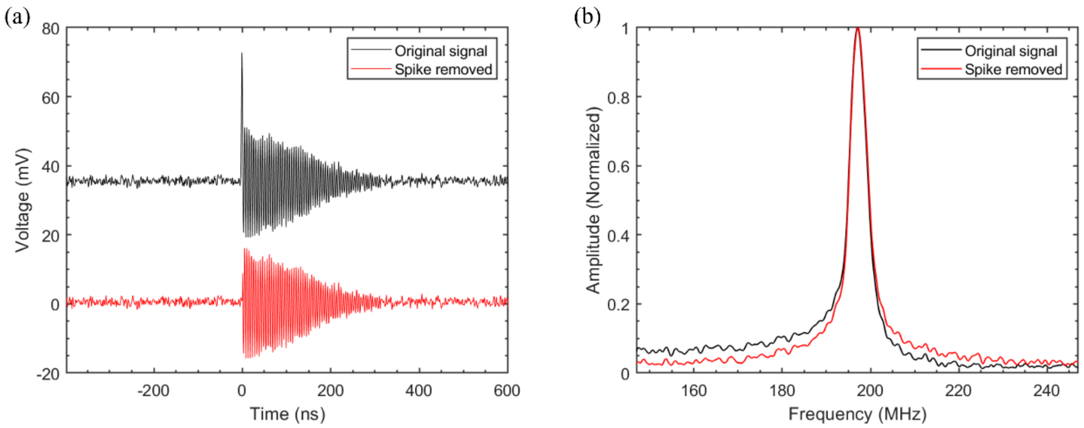

Figure 5.2 (a) ISBS signal of the 1 M sucrose solution in the time domain before spike filtering (black, offset of +35 mV added for clarity) and after (red). (b) FFTs of the same ISBS signals.

5.3.2. ISBS data fitting and results

Curve-fitting on the frequency-domain ISBS data was conducted using the standard Lorentzian fit (Equation 5.2) as well as the custom-fit function (Equation 5.1) for each of the prepared aqueous solutions. The ISBS peaks were first fit with the Lorentzian profile, and an example of the fit compared to the data is displayed in Figure 5.3(a). The Lorentzian profile was found to fit the peak value well, but the profile was not fit as well due to the wings at the base of the profile. Figure 5.3(b) displays the custom-fit applied to the same data set. The Gaussian contribution was found to improve the fit at the base of the profile. The custom-fit was also found to fit the peak frequency value just as well as the Lorentzian fit.

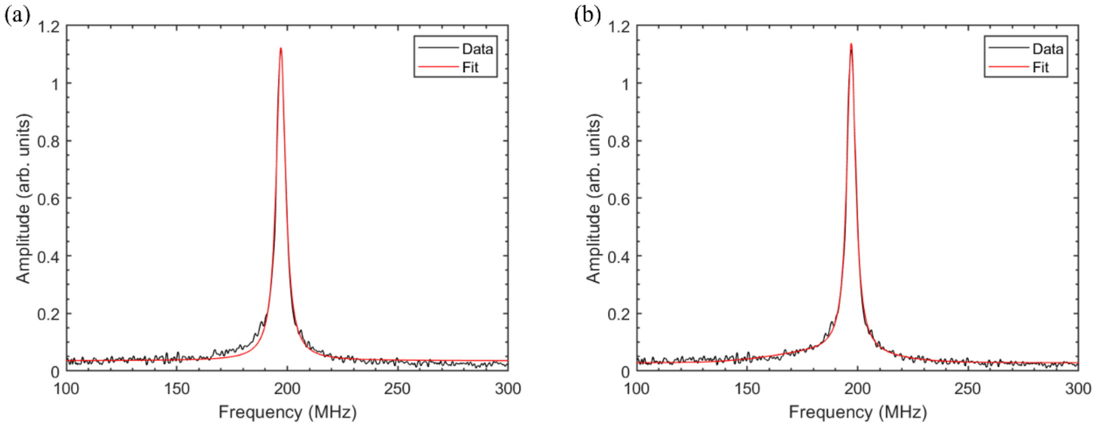

Figure 5.3 Curve-fitting results on a sample of 1 M sucrose solution while using the (a) Lorentzian fit and (b) the custom fit. Data is shown in black while the curve-fit is shown in red.

Following the curve-fitting procedure with the two fitting functions, the goodness of fit was evaluated by computing the ratio of their SSR values with Equation 5.3. Figure 5.4 displays the mean $\mathrm{SSR}_{\mathrm{ratio}}$ values ($n = 5$ replicates) computed for each sample at each dilution state with the standard deviation used as the error bars. The mean $\mathrm{SSR}_{\mathrm{ratio}}$ values for all samples were found to be between 0.575 and 0.696 for these samples. Based on how $\mathrm{SSR}_{\mathrm{ratio}}$ was previously defined, the custom-fit function has a smaller SSR value than the Lorentzian fit when the ratio is less than 1. Therefore, the custom-fit function was found to fit the data closer than the Lorentzian fit for each solution based on the results displayed in Figure 5.4. This is in agreement with the qualitative assessment of the two fits from figures such as Figure 5.3. Prior to taking the mean values of each ratio, the highest and lowest SSR ratio values were found to be 0.888 and 0.437, respectively. Therefore, the custom-fit function provided a closer fitting model for the bio-relevant solution data for all replicate measurements of each solution taken for this assessment.

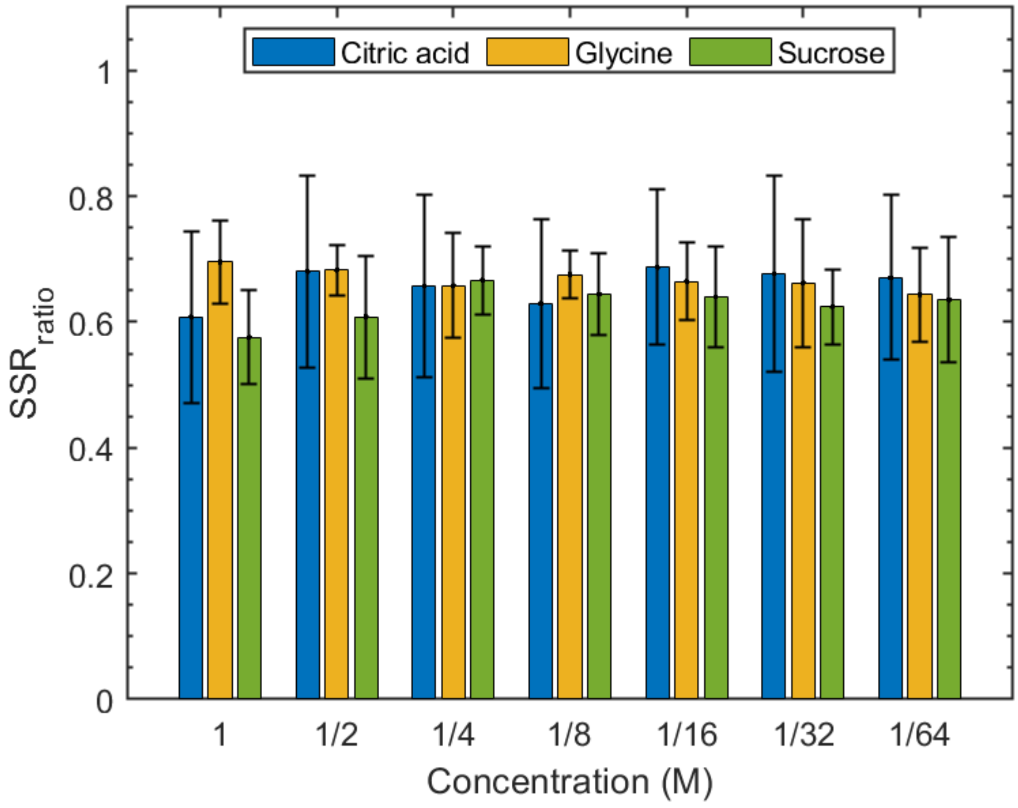

Figure 5.4 Bar chart displaying the SSR ratio values for the solutions of citric acid (blue), glycine (yellow), and sucrose (green).

5.3.3. Effects of initial pump diameter on signal damping and linewidth

The pump beam diameter was expanded using two lenses before the PBS cube (see Fig. 5.1) with the lens choices listed in Table 5.1. Figure 5.5(a) displays the set of normalized ISBS signals obtained with acetone for different pump diameters (d_{pump}). The damping of the ISBS signal was observed to decreased with increasing pump diameter, and vice-versa. This pump geometry dependent damping behavior in the time domain has been observed in previous ISBS studies involving theoretical simulations [21] and experiments with methanol [19]. Both studies concluded that the signal damping decreased with increasing pump spot size at the sample, specifically in the x-direction. In our setup, increasing the d_{pump} increases the x-direction spot size at the grating, since our setup employs the use of a cylindrical lens to focus the pump in the y-direction (See Figure 5.1). Therefore, an increased d_{pump} is imaged by the f_5/f_6 telescope to a larger x-direction spot size at the sample. Since an increase in d_{pump} resulted in less signal damping in our data and corresponds to a larger x-direction spot size at the focus for our setup, we conclude that the observed results in Figure 5.5(a) are consistent with the results presented in the previous studies.

Figure 5.5(b) displays the normalized FFTs of the same acetone signals from Figure 5.5(a). The linewidth of the signal was observed to consistently decrease with increasing pump diameter, and vice-versa. To our knowledge, these results provide the first demonstration of ISBS instrumentation affecting the linewidth and subsequently the spectral resolution of the ISBS signals in the Fourier domain. These results indicate that the spectral resolution of the peaks can be increased by increasing the pump beam diameter following emission from the laser, based on our ISBS setup as given in Figure 5.1.

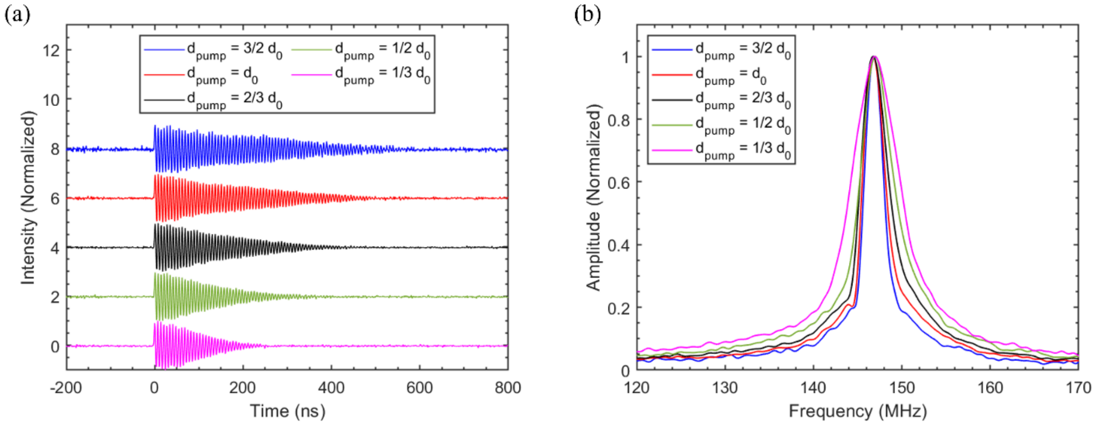

Figure 5.5 (a) Normalized ISBS signals from acetone in the time domain with varying pump beam diameters. (b) Normalized FFTs of the same ISBS signals.

The Fourier domain signals for acetone from Figure 5(b) were all fit using Equation 5.1, and the FWHM values as a function of the relative beam diameter (d_{pump}/d_0) are displayed in Figure 5.6(a). In addition, the narrowest spectral resolution for the current state-of-the-art for ISBS is displayed as a dashed line at 3 MHz [119]. The FWHM of the peak appears to decrease in exponential fashion with increasing pump beam diameter. At the largest pump diameter $d_{pump} = \frac{3}{2}d_0$, the spectral resolution was found to be approximately 2.5 MHz, which improves upon the current state-of-the-art for ISBS. In addition, Figure 5.6(b) displays the peak frequency value as a function of the relative pump diameter. The peak frequency was found to not change appreciably for the different pump beam diameters. Therefore, we further conclude that the pump diameter can be increased or decreased while maintaining the sample's expected ISBS frequency value.

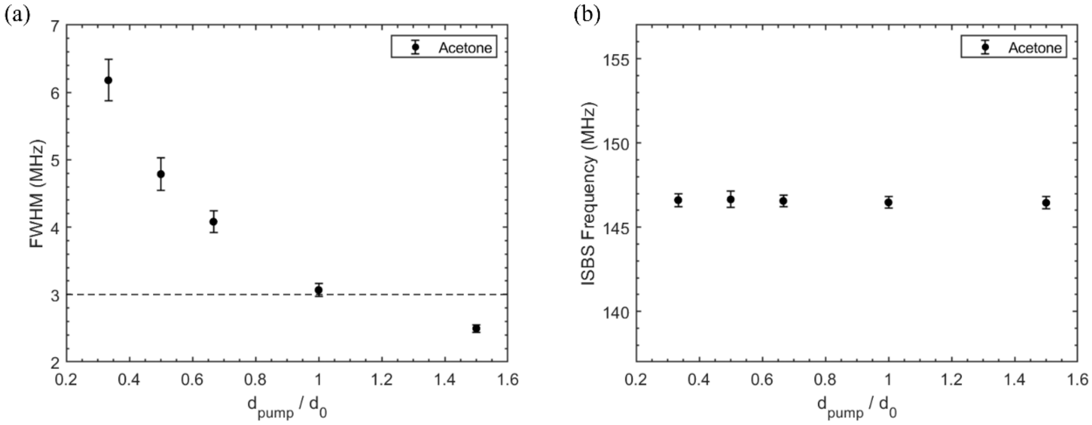

Figure 5.6 (a) FWHM and (b) peak frequencies from the curve-fits used to fit the acetone data (n = 3 replicate runs), as a function of the relative pump diameter. The dashed line in (a) represents the lower bound for ISBS spectral resolution reported previously [119].

5.4. Discussion

In a recent assessment of Brillouin techniques [119], the state-of-the-art spectral resolution of ISBS was reported to be 3 – 6 MHz. As we demonstrate in our results, pump beam expansion can allow for a spectral resolution of less than 3 MHz which is better than the currently reported state-of-the-art. Our current setup limitation for expanding the pump beam is the dimensions of our polarized beam splitter cube, which is used to control the polarization of our pump pulses. The half inch sides limit our ability to further expand the pump beam diameter beyond 1.5 times the initial pump diameter. With a PBS cube of 1-inch sides, we anticipate that the spectral resolution can be further improved while still maintaining control of the pump pulse polarization with the given setup configuration.

One of the issues that can arise when expanding the pump and probe beams is the subsequent expansion of the pump and probe profiles at the Fourier plane of the 4f telescope following the transmission grating. This results in a horizontal overlap of the pump and probe profiles at the Fourier plane that occurs at both the +1 and -1 diffraction modes which would limit the system to strictly the heterodyne detection scheme. From our experimental observations, an advantage of using the cylindrical lens to focus the pump pulses before the grating is that the pump pulses have a vertical line spatial geometry at the Fourier plane which limits its horizontal spread. By applying the use of a cylindrical lens to focus both the pump and the probe, the beam geometries can be expanded and the vertical spatial geometries at the Fourier plane can allow for separation of the pump and probe profiles at the +1 and -1 diffraction modes, allowing for the choice of heterodyne or homodyne detection schemes.

5.5. Conclusion

We have demonstrated that the instrumentation in ISBS experiments can affect the linewidth in the Fourier domain. Expanding the pump beam diameter with our setup resulted in a decrease in the ISBS signal linewidth. In addition, we have demonstrated that pump diameter variation can produce a Fourier domain signal with sub-3 MHz FWHM, which improves upon the current state-of-the-art of ISBS spectral resolution [119]. The ISBS peak frequency was not appreciably changed by the different pump diameters. In addition to these results on spectral resolution, we also demonstrated the effect of spike artifact removal on the ISBS signal symmetry, and we introduced a custom-fitting function that can provide a closer fit for the ISBS profile than the Lorentzian fit. By combining these pump shaping methods with the recently reported methodologies for improving lateral resolution [24], we believe that ISBS microscopy with high spectral and spatial resolution for biomedical applications is possible.

6. CONCLUSION

6.1. Summary

In summary, this work presents the application of different nonlinear spectroscopic techniques in many biomedical fields, such as laser-eye safety standards, the origins of photobiomodulation, and organ-on-a-chip studies.

In chapter 2, open-air filamentation using near-IR femtosecond pulses was studied, and supercontinuum generation and high harmonic generation was observed in the spectral output following the optical filament. We demonstrated that the sub-1000 nm light generated following the filament presented an eye-safety hazard according to the ANSI standards for Safe Use of Lasers Z136.1-2014 [51].

In chapter 3, we introduce a modified TAS system, called CW-TAS, to study proteins with TAS while simultaneously applying CW light onto the sample. We demonstrated that the electronic processes measured by TAS of the protein reduced cytochrome c were not changed or degraded because of the CW light. This both eliminates those processes as potential initiators of the PBM effect as well as establishes the proof-of-principle for CW-TAS as a technique to study PBM effects without degradation of the sample or data.

In chapter 4, we apply the CW-TAS technique to the more complicated protein Complex III as well as test with standard TAS methodologies. We present the first TAS time constants for redox states of Complex III from specifically a mammalian source, and we also demonstrate with CW-TAS that 635 nm light did not have an effect on the electronic transitions probed by TAS. The elimination of these mechanisms leads to a better understanding of the origin of the photobiomodulation effect.

In chapter 5, we investigated the influence of the initial pump beam geometry on the frequency and linewidth of ISBS signal. We demonstrated that the linewidth of the Fourier domain ISBS signal was found to be dependent on the initial pump beam diameter while the frequency remained the same. By expanding the initial pump beam diameter and using a cylindrical lens to focus the pump pulses, the spectral resolution of ISBS measurements can be improved allowing for higher resolvability of two close signals.

6.2. Future Work

While CW-TAS has been introduced as an ultrafast nonlinear technique as a possible technique to further study the initiation of the PBM effect, the mechanisms of PBM are still not well understood. A potential future direction with this technique would be to study Complex IV (C-IV), the protein that is hypothesized to be the central photoacceptor for PBM [78,80]. C-IV has been previously characterized with the TAS technique where the photodissociation of nitric oxide (NO) (and recombination?) had been characterized [95]. One of the main hypotheses for what initiates PBM, the redox modulation hypothesis [77], involves the binding and dissociation of NO from C-IV and its effect on the activity of C-IV. CW-TAS experiments with either isolated C-IV or C-IV in a protein supercomplex may help to further elucidate the effect of CW light on the photodissociation of NO from C-IV and the corresponding effect that may have on other electronic processes occurring in C-IV.

REFERENCES

1. T. H. Maiman, "Stimulated Optical Radiation in Ruby," Nature **187**(4736), 493–494 (1960).

2. A. L. Schawlow and C. H. Townes, "Infrared and Optical Masers," Phys. Rev. **112**(6), 1940–1949 (1958).

3. P. A. Franken, A. E. Hill, C. W. Peters, and G. Weinreich, "Generation of Optical Harmonics," Phys. Rev. Lett. **7**(4), 118–119 (1961).

4. R. W. Boyd, *Nonlinear Optics* (Academic Press, 2008).

5. P. L. Kelley, "Self-Focusing of Optical Beams," Phys. Rev. Lett. **15**(26), 1005–1008 (1965).

6. R. G. Brewer, "Frequency Shifts in Self-Focused Light," Phys. Rev. Lett. **19**(1), 8–10 (1967).

7. F. Shimizu, "Frequency Broadening in Liquids by a Short Light Pulse," Phys. Rev. Lett. **19**(19), 1097–1100 (1967).

8. F. DeMartini, C. H. Townes, T. K. Gustafson, and P. L. Kelley, "Self-Steepening of Light Pulses," Phys. Rev. **164**(2), 312–323 (1967).

9. R. Y. Chiao, E. Garmire, and C. H. Townes, "Self-Trapping of Optical Beams," Phys. Rev. Lett. **13**(15), 479–482 (1964).

10. A. Couairon and A. Mysyrowicz, "Femtosecond filamentation in transparent media," Phys. Rep. **441**(2–4), 47–189 (2007).

11. E. T. J. Nibbering, G. Grillon, M. A. Franco, B. S. Prade, and A. Mysyrowicz,

"Determination of the inertial contribution to the nonlinear refractive index of air, N_2, and O_2 by use of unfocused high-intensity femtosecond laser pulses," J. Opt. Soc. Am. B **14**(3), 650 (1997).

12. P. P. Ho and R. R. Alfano, "Optical Kerr effect in liquids," Phys. Rev. A **20**(5), 2170–2187 (1979).
13. R. DeSalvo, A. A. Said, D. J. Hagan, E. W. Van Stryland, and M. Sheik-Bahae, "Infrared to ultraviolet measurements of two-photon absorption and n/sub 2/ in wide bandgap solids," IEEE J. Quantum Electron. **32**(8), 1324–1333 (1996).
14. P. Kabaciński, T. M. Kardaś, Y. Stepanenko, and C. Radzewicz, "Nonlinear refractive index measurement by SPM-induced phase regression," Opt. Express **27**(8), 11018 (2019).
15. A. A. Said, M. Sheik-Bahae, D. J. Hagan, T. H. Wei, J. Wang, J. Young, and E. W. Van Stryland, "Determination of bound-electronic and free-carrier nonlinearities in ZnSe, GaAs, CdTe, and ZnTe," J. Opt. Soc. Am. B **9**(3), 405 (1992).
16. A. V. Mitrofanov, A. A. Voronin, D. A. Sidorov-Biryukov, A. Pugžlys, E. A. Stepanov, G. Andriukaitis, T. Flöry, S. Ališauskas, A. B. Fedotov, A. Baltuška, and A. M. Zheltikov, "Mid-infrared laser filaments in the atmosphere," Sci. Rep. **5**(1), 8368 (2015).
17. T. Auguste, P. Monot, L.-A. Lompré, G. Mainfray, and C. Manus, "Defocusing effects of a picosecond terawatt laser pulse in an underdense plasma," Opt. Commun. **89**(2–4), 145–148 (1992).
18. R. Berera, R. van Grondelle, and J. T. M. Kennis, "Ultrafast transient absorption

spectroscopy: principles and application to photosynthetic systems," Photosynth. Res. **101**(2–3), 105–118 (2009).

19. P. Bartolini, A. Taschin, R. Eramo, and R. Torre, "Transient Grating Experiments in Glass-Former Liquids," in *Time-Resolved Spectroscopy in Complex Liquids* (Springer US, 2008), pp. 129–184.
20. H. J. Eichler, P. Günter, and D. W. Pohl, *Laser-Induced Dynamic Gratings*, Springer Series in Optical Sciences (Springer Berlin Heidelberg, 1986), **50**(11).
21. Y. Yan and K. A. Nelson, "Impulsive stimulated light scattering. I. General theory," J. Chem. Phys. **87**(11), 6240–6256 (1987).
22. Y. Yan and K. A. Nelson, "Impulsive stimulated light scattering. II. Comparison to frequency-domain light-scattering spectroscopy," J. Chem. Phys. **87**(11), 6257–6265 (1987).
23. C. W. Ballmann, Z. Meng, A. J. Traverso, M. O. Scully, and V. V. Yakovlev, "Impulsive Brillouin microscopy," Optica **4**(1), 124 (2017).
24. B. Krug, N. Koukourakis, and J. W. Czarske, "Impulsive stimulated Brillouin microscopy for non-contact, fast mechanical investigations of hydrogels," Opt. Express **27**(19), 26910 (2019).
25. B. Krug, N. Koukourakis, J. Guck, and J. Czarske, "Nonlinear microscopy using impulsive stimulated Brillouin scattering for high-speed elastography," Opt. Express **30**(4), 4748 (2022).
26. R. R. Alfano and S. L. Shapiro, "Emission in the Region 4000 to 7000 Å Via Four-Photon Coupling in Glass," Phys. Rev. Lett. **24**(11), 584–587 (1970).

27. C. P. Hauri, W. Kornelis, F. W. Helbing, A. Heinrich, A. Couairon, A. Mysyrowicz, J. Biegert, and U. Keller, "Generation of intense, carrier-envelope phase-locked few-cycle laser pulses through filamentation," Appl. Phys. B **79**(6), 673–677 (2004).

28. K. Stelmaszczyk, P. Rohwetter, G. Méjean, J. Yu, E. Salmon, J. Kasparian, R. Ackermann, J.-P. Wolf, and L. Wöste, "Long-distance remote laser-induced breakdown spectroscopy using filamentation in air," Appl. Phys. Lett. **85**(18), 3977–3979 (2004).

29. P. Rairoux, H. Schillinger, S. Niedermeier, M. Rodriguez, F. Ronneberger, R. Sauerbrey, B. Stein, D. Waite, C. Wedekind, H. Wille, L. Wöste, and C. Ziener, "Remote sensing of the atmosphere using ultrashort laser pulses," Appl. Phys. B Lasers Opt. **71**(4), 573–580 (2000).

30. J. Kasparian, M. Rodriguez, G. Méjean, J. Yu, E. Salmon, H. Wille, R. Bourayou, S. Frey, Y. B. Andre, A. Mysyrowicz, R. Sauerbrey, J. P. Wolf, and L. Wöste, "White-light filaments for atmospheric analysis.," Science **301**(5629), 61–4 (2003).

31. J.-F. Daigle, A. Jaroń-Becker, S. Hosseini, T.-J. Wang, Y. Kamali, G. Roy, A. Becker, and S. L. Chin, "Intensity clamping measurement of laser filaments in air at 400 and 800 nm," Phys. Rev. A **82**(2), 023405 (2010).

32. I. Hartl, X. D. Li, C. Chudoba, R. K. Ghanta, T. H. Ko, J. G. Fujimoto, J. K. Ranka, and R. S. Windeler, "Ultrahigh-resolution optical coherence tomography using continuum generation in an air–silica microstructure optical fiber," Opt. Lett. **26**(9), 608 (2001).

33. G. I. Petrov, A. Doronin, H. T. Whelan, I. Meglinski, and V. V. Yakovlev, "Human tissue color as viewed in high dynamic range optical spectral transmission measurements," Biomed. Opt. Express **3**(9), 2154 (2012).

34. D. Wildanger, E. Rittweger, L. Kastrup, and S. W. Hell, "STED microscopy with a supercontinuum laser source," Opt. Express **16**(13), 9614 (2008).

35. S. A. Kovalenko, A. L. Dobryakov, J. Ruthmann, and N. P. Ernsting, "Femtosecond spectroscopy of condensed phases with chirped supercontinuum probing," Phys. Rev. A **59**(3), 2369–2384 (1999).

36. S. P. O'Connor, J. W. Lalonde, J. M. Rickman, G. D. Noojin, N. J. Pope, M. L. Denton, M. O. Scully, and V. V. Yakovlev, "Investigation of reaction mechanisms of cytochrome c and mitochondria with transient absorption spectroscopy," in *Mechanisms of Photobiomodulation Therapy XIV*, M. R. Hamblin, J. D. Carroll, and P. Arany, eds. (SPIE, 2019), (March), p. 14.

37. G. I. Petrov and V. V. Yakovlev, "Enhancing red-shifted white-light continuum generation in optical fibers for applications in nonlinear Raman microscopy," Opt. Express **13**(4), 1299 (2005).

38. H. Kano and H. Hamaguchi, "Dispersion-compensated supercontinuum generation for ultrabroadband multiplex coherent anti-Stokes Raman scattering spectroscopy," J. Raman Spectrosc. **37**(1–3), 411–415 (2006).

39. Y. Shen, A. A. Voronin, A. M. Zheltikov, S. P. O'Connor, V. V. Yakovlev, A. V. Sokolov, and M. O. Scully, "Supercontinuum generation in large-mode-area photonic crystal fibers for coherent Raman microspectroscopy," in *Frontiers in*

Ultrafast Optics: Biomedical, Scientific, and Industrial Applications XVIII, P. R. Herman, M. Meunier, and R. Osellame, eds. (SPIE, 2018), (February), p. 16.

40. Y. Shen, A. A. Voronin, A. M. Zheltikov, S. P. O'Connor, V. V. Yakovlev, A. V. Sokolov, and M. O. Scully, "Picosecond supercontinuum generation in large mode area photonic crystal fibers for coherent anti-Stokes Raman scattering microspectroscopy," Sci. Rep. **8**(1), 9526 (2018).
41. A. Braun, G. Korn, X. Liu, D. Du, J. Squier, and G. Mourou, "Self-channeling of high-peak-power femtosecond laser pulses in air," Opt. Lett. **20**(1), 73 (1995).
42. C. P. Hauri, R. B. Lopez-Martens, C. I. Blaga, K. D. Schultz, J. Cryan, R. Chirla, P. Colosimo, G. Doumy, A. M. March, C. Roedig, E. Sistrunk, J. Tate, J. Wheeler, L. F. DiMauro, and E. P. Power, "Intense self-compressed, self-phase-stabilized few-cycle pulses at 2 μm from an optical filament," Opt. Lett. **32**(7), 868 (2007).
43. A. A. Voronin, S. Ališauskas, O. D. Mücke, A. Pugžlys, A. Baltuška, and A. M. Zheltikov, "High-energy-throughput pulse compression by off-axis group-delay compensation in a laser-induced filament," Phys. Rev. A **84**(2), 023832 (2011).
44. L. Haizer, I. Bugar, E. Serebryannikov, D. Lorenc, F. Uherek, E. Goulielmakis, and A. Zheltikov, "Intense Cr:forsterite-laser-based supercontinuum source," Opt. Lett. **39**(19), 5562 (2014).
45. S. Driever, D. Bigourd, N. Fedorov, M. Cornet, M. Arnold, F. Burgy, S. Montant, S. Petit, D. Descamps, E. Cormier, E. Constant, and A. Zaïr, "Tunable 1.6–2 μ m near infrared few-cycle pulse generation by filamentation," Appl. Phys. Lett. **102**(19), 191119 (2013).

46. S. Tzortzakis, B. Lamouroux, A. Chiron, S. D. Moustaizis, D. Anglos, M. Franco, B. Prade, and A. Mysyrowicz, "Femtosecond and picosecond ultraviolet laser filaments in air: experiments and simulations," Opt. Commun. **197**(1–3), 131–143 (2001).

47. B. Prade, M. Franco, A. Mysyrowicz, A. Couairon, H. Buersing, B. Eberle, M. Krenz, D. Seiffer, and O. Vasseur, "Spatial mode cleaning by femtosecond filamentation," Conf. Lasers Electro-Optics 2006 Quantum Electron. Laser Sci. Conf. CLEO/QELS 2006 **31**(17), 2601–2603 (2006).

48. D. Mikalauskas, A. Dubietis, and R. Danielius, "Observation of light filaments induced in air by visible picosecond laser pulses," Appl. Phys. B Lasers Opt. **75**(8), 899–902 (2002).

49. A. V Mitrofanov, A. A. Voronin, G. Andriukaitis, T. Flöry, and A. Pug, "Post-filament self-trapping of ultrashort laser pulses," **39**(16), 4659–4662 (2014).

50. S. Tochitsky, E. Welch, M. Polyanskiy, I. Pogorelsky, P. Panagiotopoulos, M. Kolesik, E. M. Wright, S. W. Koch, J. V Moloney, J. Pigeon, and C. Joshi, "Megafilament in air formed by self-guided terawatt long-wavelength infrared laser," Nat. Photonics **13**(January), 41–46 (2019).

51. *American National Standard for Safe Use of Lasers: ANSI Z136.1–2014* (Laser Institute of America, 2014).

52. C. B. Marble, S. P. O’Connor, D. T. Nodurft, A. W. Wharmby, and V. V. Yakovlev, "Eye safety implications of high harmonic generation in zinc selenide," Opt. Express **27**(3), 2828 (2019).

53. C. B. Marble, S. P. O’Connor, D. T. Nodurft, V. V. Yakovlev, and A. W. Wharmby, "Visible supercontinuum generation from a tunable mid-infrared laser," in *Nonlinear Frequency Generation and Conversion: Materials and Devices XVII*, K. L. Vodopyanov and K. L. Schepler, eds. (SPIE, 2018), **10516**(February), p. 19.

54. V. V. Yakovlev, B. Kohler, and K. R. Wilson, "Broadly tunable 30-fs pulses produced by optical parametric amplification," Opt. Lett. **19**(23), 2000 (1994).

55. K. R. Wilson and V. V. Yakovlev, "Ultrafast rainbow: tunable ultrashort pulses from a solid-state kilohertz system," J. Opt. Soc. Am. B **14**(2), 444 (1997).

56. A. M. Weiner, *Ultrafast Optics* (John Wiley & Sons, Inc., 2009).

57. E. T. J. Nibbering, P. F. Curley, G. Grillon, B. S. Prade, M. A. Franco, F. Salin, and A. Mysyrowicz, "Conical emission from self-guided femtosecond pulses in air," Opt. Lett. **21**(1), 62 (1996).

58. O. G. Kosareva, V. P. Kandidov, A. Brodeur, C. Y. Chien, and S. L. Chin, "Conical emission from laser–plasma interactions in the filamentation of powerful ultrashort laser pulses in air," Opt. Lett. **22**(17), 1332 (1997).

59. S. Passarella, E. Casamassima, S. Molinari, D. Pastore, E. Quagliariello, I. M. Catalano, and A. Cingolani, "Increase of proton electrochemical potential and ATP synthesis in rat liver mitochondria irradiated in vitro by helium-neon laser," FEBS Lett. **175**(1), 95–99 (1984).

60. N. M. Khalil and M. G. Noureldin, "Comparison of Single Versus Multiple Low-Level Laser Applications on Bone Formation in Extraction Socket Healing in Rabbits (Histologic and Histomorphometric Study)," J. Oral Maxillofac. Surg.

77(9), 1760–1768 (2019).

61. C. F. Rizzi, J. L. Mauriz, D. S. Freitas Corrêa, A. J. Moreira, C. G. Zettler, L. I. Filippin, N. P. Marroni, and J. González-Gallego, "Effects of low-level laser therapy (LLLT) on the nuclear factor (NF)-κB signaling pathway in traumatized muscle," Lasers Surg. Med. **38**(7), 704–713 (2006).
62. T. De Marchi, E. C. P. Leal Junior, C. Bortoli, S. S. Tomazoni, R. Á. B. Lopes-Martins, and M. Salvador, "Low-level laser therapy (LLLT) in human progressive-intensity running: effects on exercise performance, skeletal muscle status, and oxidative stress," Lasers Med. Sci. **27**(1), 231–236 (2012).
63. C. B. Lopes, A. L. B. Pinheiro, S. Sathaiah, N. S. Da Silva, and M. A. C. Salgado, "Infrared Laser Photobiomodulation (λ 830 nm) on Bone Tissue Around Dental Implants: A Raman Spectroscopy and Scanning Electronic Microscopy Study in Rabbits," Photomed. Laser Surg. **25**(2), 96–101 (2007).
64. N. J. Pope, S. M. Powell, J. C. Wigle, and M. L. Denton, "Wavelength- and irradiance-dependent changes in intracellular nitric oxide level," J. Biomed. Opt. **25(**08), 1 (2020).
65. P. V Peplow, T. Chung, and G. D. Baxter, "Laser Photobiomodulation of Wound Healing: A Review of Experimental Studies in Mouse and Rat Animal Models," Photomed. Laser Surg. **28**(3), 291–325 (2010).
66. A. V. Corazza, J. Jorge, C. Kurachi, and V. S. Bagnato, "Photobiomodulation on the Angiogenesis of Skin Wounds in Rats Using Different Light Sources," Photomed. Laser Surg. **25**(2), 102–106 (2007).

67. R. T. Chow and P. J. Armati, "Photobiomodulation: Implications for Anesthesia and Pain Relief," Photomed. Laser Surg. **34**(12), 599–609 (2016).

68. M. F. X. B. Cavalcanti, U. H. Silva, E. C. P. Leal-Junior, R. A. B. Lopes-Martins, R. L. Marcos, R. C. Pallotta, F. Diomede, O. Trubiani, N. De Isla, and L. Frigo, "Comparative Study of the Physiotherapeutic and Drug Protocol and Low-Level Laser Irradiation in the Treatment of Pain Associated with Temporomandibular Dysfunction," Photomed. Laser Surg. **34**(12), 652–656 (2016).

69. M. F. X. B. Cavalcanti, D. A. Maria, N. de Isla, E. C. P. Leal-Junior, J. Joensen, J. M. Bjordal, R. A. M. B. Lopes-Martins, F. Diomede, O. Trubiani, and L. Frigo, "Evaluation of the Proliferative Effects Induced by Low-Level Laser Therapy in Bone Marrow Stem Cell Culture," Photomed. Laser Surg. **33**(12), 610–616 (2015).

70. F. M. de Lima, A. B. Villaverde, R. Albertini, J. C. Corrêa, R. L. P. Carvalho, E. Munin, T. Araújo, J. A. Silva, and F. Aimbire, "Dual Effect of low-level laser therapy (LLLT) on the acute lung inflammation induced by intestinal ischemia and reperfusion: Action on anti- and pro-inflammatory cytokines," Lasers Surg. Med. **43**(5), 410–420 (2011).

71. P. Douris, V. Southard, R. Ferrigi, J. Grauer, D. Katz, C. Nascimento, and P. Podbielski, "Effect of Phototherapy on Delayed Onset Muscle Soreness," Photomed. Laser Surg. **24**(3), 377–382 (2006).

72. C. Ferraresi, M. V. P. de Sousa, Y.-Y. Huang, V. S. Bagnato, N. A. Parizotto, and M. R. Hamblin, "Time response of increases in ATP and muscle resistance to fatigue after low-level laser (light) therapy (LLLT) in mice," Lasers Med. Sci.

30(4), 1259–1267 (2015).

73. J. J. Anders, S. Geuna, and S. Rochkind, "Phototherapy promotes regeneration and functional recovery of injured peripheral nerve," Neurol. Res. **26**(2), 233–239 (2004).

74. J. J. Anders, H. Moges, X. Wu, I. D. Erbele, S. L. Alberico, E. K. Saidu, J. T. Smith, and B. A. Pryor, "In vitro and in vivo optimization of infrared laser treatment for injured peripheral nerves," Lasers Surg. Med. **46**(1), 34–45 (2014).

75. K. R. Byrnes, R. W. Waynant, I. K. Ilev, X. Wu, L. Barna, K. Smith, R. Heckert, H. Gerst, and J. J. Anders, "Light promotes regeneration and functional recovery and alters the immune response after spinal cord injury," Lasers Surg. Med. **36**(3), 171–185 (2005).

76. M. R. Hamblin, "Photobiomodulation for traumatic brain injury and stroke," J. Neurosci. Res. **96**(4), 731–743 (2018).

77. S. Passarella and T. Karu, "Absorption of monochromatic and narrow band radiation in the visible and near IR by both mitochondrial and non-mitochondrial photoacceptors results in photobiomodulation," J. Photochem. Photobiol. B Biol. **140**, 344–358 (2014).

78. L. F. de Freitas and M. R. Hamblin, "Proposed Mechanisms of Photobiomodulation or Low-Level Light Therapy," IEEE J. Sel. Top. Quantum Electron. **22**(3), 348–364 (2016).

79. T. Karu, "Mitochondrial Mechanisms of Photobiomodulation in Context of New Data About Multiple Roles of ATP," Photomed. Laser Surg. **28**(2), 159–160

(2010).

80. T. I. Karu, "Cellular and Molecular Mechanisms of Photobiomodulation (Low-Power Laser Therapy)," IEEE J. Sel. Top. Quantum Electron. **20**(2), 143–148 (2014).

81. J. T. Eells, M. T. T. Wong-Riley, J. VerHoeve, M. Henry, E. V. Buchman, M. P. Kane, L. J. Gould, R. Das, M. Jett, and B. D. Hodgson, "Mitochondrial signal transduction in accelerated wound and retinal healing by near-infrared light therapy," Mitochondrion **4**(5–6), 559–567 (2004).

82. T. I. Karu, L. V. Pyatibrat, G. S. Kalendo, and R. O. Esenaliev, "Effects of monochromatic low-intensity light and laser irradiation on adhesion of HeLa cells in vitro," Lasers Surg. Med. **18**(2), 171–177 (1996).

83. T. I. Karu, "Mitochondrial Signaling in Mammalian Cells Activated by Red and Near-IR Radiation," Photochem. Photobiol. **84**(5), 1091–1099 (2008).

84. Y. Liu, G. Fiskum, and D. Schubert, "Generation of reactive oxygen species by the mitochondrial electron transport chain," J. Neurochem. **80**(5), 780–787 (2002).

85. J. T. Hashmi, Y. Huang, B. Z. Osmani, S. K. Sharma, M. A. Naeser, and M. R. Hamblin, "Role of Low-Level Laser Therapy in Neurorehabilitation," PM&R **2**(12S), (2010).

86. R. Giovannetti, "The Use of Spectrophotometry UV-Vis for the Study of Porphyrins," in *Macro To Nano Spectroscopy* (InTech, 2012).

87. J. L. Martin and M. H. Vos, "Femtosecond Biology," Annu. Rev. Biophys. Biomol. Struct. **21**(1), 199–222 (1992).

88. M. H. Vos, "Ultrafast dynamics of ligands within heme proteins," Biochim. Biophys. Acta - Bioenerg. **1777**(1), 15–31 (2008).

89. A. P. Sommer, P. Schemmer, A. E. Pavláth, H.-D. Försterling, Á. R. Mester, and M. A. Trelles, "Quantum biology in low level light therapy: death of a dogma," Ann. Transl. Med. **8**(7), 440–440 (2020).

90. A. A. P. Chauvet, A. Al Haddad, W.-C. Kao, F. van Mourik, C. Hunte, and M. Chergui, "Photo-induced dynamics of the heme centers in cytochrome bc 1," Phys. Chem. Chem. Phys. **17**(3), 2143–2151 (2015).

91. M. H. Vos, B. J. Reeder, F. Daldal, and U. Liebl, "Ultrafast photochemistry of the bc 1 complex," Phys. Chem. Chem. Phys. **19**(9), 6807–6813 (2017).

92. W. Wang, X. Ye, A. A. Demidov, F. Rosca, T. Sjodin, W. Cao, M. Sheeran, and P. M. Champion, "Femtosecond Multicolor Pump−Probe Spectroscopy of Ferrous Cytochrome c †," J. Phys. Chem. B **104**(46), 10789–10801 (2000).

93. M. Negrerie, S. Cianetti, M. H. Vos, J. Martin, and S. G. Kruglik, "Ultrafast Heme Dynamics in Ferrous versus Ferric Cytochrome c Studied by Time-Resolved Resonance Raman and Transient Absorption Spectroscopy," J. Phys. Chem. B **110**(25), 12766–12781 (2006).

94. D. Löwenich, K. Kleinermanns, V. Karunakaran, and S. A. Kovalenko, "Transient and stationary spectroscopy of cytochrome c: ultrafast internal conversion controls photoreduction.," Photochem. Photobiol. **84**(1), 193–201 (2008).

95. M. H. Vos, G. Lipowski, J.-C. Lambry, J.-L. Martin, and U. Liebl, "Dynamics of Nitric Oxide in the Active Site of Reduced Cytochrome c Oxidase aa 3,"

Biochemistry **40**(26), 7806–7811 (2001).

96. T. F. Johnston, "Beam propagation (M^2) measurement made as easy as it gets: the four-cuts method," Appl. Opt. **37**(21), 4840 (1998).

97. P. J. M. Johnson, V. I. Prokhorenko, and R. J. D. Miller, "Stable UV to IR supercontinuum generation in calcium fluoride with conserved circular polarization states," Opt. Express **17**(24), 21488 (2009).

98. I. H. M. van Stokkum, D. S. Larsen, and R. van Grondelle, "Global and target analysis of time-resolved spectra," Biochim. Biophys. Acta - Bioenerg. **1657**(2–3), 82–104 (2004).

99. C. Ruckebusch, M. Sliwa, P. Pernot, A. de Juan, and R. Tauler, "Comprehensive data analysis of femtosecond transient absorption spectra: A review," J. Photochem. Photobiol. C Photochem. Rev. **13**(1), 1–27 (2012).

100. S. G. Kruglik, B.-K. Yoo, J.-C. Lambry, J.-L. Martin, and M. Negrerie, "Structural changes and picosecond to second dynamics of cytochrome c in interaction with nitric oxide in ferrous and ferric redox states," Phys. Chem. Chem. Phys. **19**(32), 21317–21334 (2017).

101. Y. Wang, Y.-Y. Huang, Y. Wang, P. Lyu, and M. R. Hamblin, "Red (660 nm) or near-infrared (810 nm) photobiomodulation stimulates, while blue (415 nm), green (540 nm) light inhibits proliferation in human adipose-derived stem cells," Sci. Rep. **7**(1), 7781 (2017).

102. N. J. Pope and M. L. Denton, "Low irradiance light exposure alters the activity of key enzymes in the mitochondrial electron transport chain," in *Mechanisms of*

Photobiomodulation Therapy XV, M. R. Hamblin, J. D. Carroll, and P. Arany, eds. (SPIE, 2020), (March), p. 13.

103. S. P. O’Connor, S. M. Powell, J. M. Rickman, N. J. Pope, G. D. Noojin, M. O. Scully, M. L. Denton, and V. V. Yakovlev, "Transient absorption spectroscopy to explore cellular pathways to photobiomodulation," J. Photochem. Photobiol. B Biol. **222**, 112271 (2021).

104. E. Collini, C. Ferrante, and R. Bozio, "Influence of Excitonic Interactions on the Transient Absorption and Two-Photon Absorption Spectra of Porphyrin J-Aggregates in the NIR Region," J. Phys. Chem. C **111**(50), 18636–18645 (2007).

105. P. Riccio, H. Schägger, W. D. Engel, and G. Von Jagow, "bc1-complex from beef heart, one-step purification by hydroxyapatite chromatography in triton X-100, polypeptide pattern and respiratory chain characteristics," Biochim. Biophys. Acta - Bioenerg. **459**(2), 250–262 (1977).

106. C. Consani, O. Bräm, F. van Mourik, A. Cannizzo, and M. Chergui, "Energy transfer and relaxation mechanisms in Cytochrome c," Chem. Phys. **396**(1), 108–115 (2012).

107. G. Scarcelli and S. H. Yun, "Confocal Brillouin microscopy for three-dimensional mechanical imaging," Nat. Photonics **2**(1), 39–43 (2008).

108. Z. Meng, A. J. Traverso, C. W. Ballmann, M. A. Troyanova-Wood, and V. V. Yakovlev, "Seeing cells in a new light: a renaissance of Brillouin spectroscopy," Adv. Opt. Photonics **8**(2), 300 (2016).

109. F. Palombo and D. Fioretto, "Brillouin Light Scattering: Applications in

Biomedical Sciences," Chem. Rev. **119**(13), 7833–7847 (2019).

110. R. Prevedel, A. Diz-Muñoz, G. Ruocco, and G. Antonacci, "Brillouin microscopy: an emerging tool for mechanobiology," Nat. Methods **16**(10), 969–977 (2019).

111. Z. Meng, A. J. Traverso, and V. V. Yakovlev, "Background clean-up in Brillouin microspectroscopy of scattering medium," Opt. Express **22**(5), 5410 (2014).

112. Z. Meng and V. V. Yakovlev, "Optimizing signal collection efficiency of the VIPA-based Brillouin spectrometer," J. Innov. Opt. Health Sci. **08**(04), 1550021 (2015).

113. A. J. Traverso, J. V. Thompson, Z. A. Steelman, Z. Meng, M. O. Scully, and V. V. Yakovlev, "Dual Raman-Brillouin Microscope for Chemical and Mechanical Characterization and Imaging," Anal. Chem. **87**(15), 7519–7523 (2015).

114. C. W. Ballmann, J. V. Thompson, A. J. Traverso, Z. Meng, M. O. Scully, and V. V. Yakovlev, "Stimulated Brillouin Scattering Microscopic Imaging," Sci. Rep. **5**(1), 18139 (2016).

115. I. Remer, R. Shaashoua, N. Shemesh, A. Ben-Zvi, and A. Bilenca, "High-sensitivity and high-specificity biomechanical imaging by stimulated Brillouin scattering microscopy," Nat. Methods **17**(9), 913–916 (2020).

116. Z. Coker, M. Troyanova-Wood, A. J. Traverso, T. Yakupov, Z. N. Utegulov, and V. V. Yakovlev, "Assessing performance of modern Brillouin spectrometers," Opt. Express **26**(3), 2400 (2018).

117. Z. Meng, G. I. Petrov, and V. V. Yakovlev, "Flow cytometry using Brillouin imaging and sensing via time-resolved optical (BISTRO) measurements," Analyst **140**(21), 7160–7164 (2015).

118. C. W. Ballmann, Z. Meng, and V. V. Yakovlev, "Nonlinear Brillouin spectroscopy: what makes it a better tool for biological viscoelastic measurements," Biomed. Opt. Express **10**(4), 1750 (2019).

119. G. Antonacci, T. Beck, A. Bilenca, J. Czarske, K. Elsayad, J. Guck, K. Kim, B. Krug, F. Palombo, R. Prevedel, and G. Scarcelli, "Recent progress and current opinions in Brillouin microscopy for life science applications," Biophys. Rev. **12**(3), 615–624 (2020).

120. G. Antonacci, M. R. Foreman, C. Paterson, and P. Török, "Spectral broadening in Brillouin imaging," Appl. Phys. Lett. **103**(22), 221105 (2013).

121. A. A. Maznev, K. A. Nelson, and J. A. Rogers, "Optical heterodyne detection of laser-induced gratings," Opt. Lett. **23**(16), 1319 (1998).

122. G. K. Wertheim, M. A. Butler, K. W. West, and D. N. E. Buchanan, "Determination of the Gaussian and Lorentzian content of experimental line shapes," Rev. Sci. Instrum. **45**(11), 1369–1371 (1974).

123. S. P. O’Connor, C. B. Marble, D. T. Nodurft, G. D. Noojin, A. R. Boretsky, A. W. Wharmby, M. O. Scully, and V. V. Yakovlev, "Filamentation in Atmospheric Air with Tunable 1100–2400 nm Near-Infrared Femtosecond Laser Source," Sci. Rep. **9**(1), 12049 (2019).

124. S. P. O’Connor, S. M. Powell, J. M. Rickman, N. J. Pope, G. D. Noojin, M. O. Scully, M. L. Denton, and V. V. Yakovlev, "Mammalian complex III heme dynamics studied with pump-probe spectroscopy and red light illuminations," Biomed. Opt. Express **12**(11), 7082 (2021).

APPENDIX A

SUPPLEMENTARY MATERIAL FOR CHAPTER 3

A.1. Determining number of replicate scans

When using CW during TAS data collection, each scan will have undergone a different duration of CW illumination. Therefore, averaging each scan number with the same scan number from multiple other replicate data collections is necessary, instead of averaging together all of the scans in one data collection. Since the signal to noise ratio is important for obtaining a good fit for the time constants with low uncertainty, we estimated how many replicate data sets were necessary to average a sufficient number of scans between collections to reduce the noise sufficiently for fitting the data with the kinetic fit equation used in TAS analysis (Equation A.1).

$$\Delta A_{\lambda}(t) = \sum_{i} A_i \exp\left[-\frac{t - t_0}{\tau_i}\right] + A_0 \qquad (\mathrm{A.1})$$

To estimate the number of data sets needed when using CW illuminations during TAS, a data collection with 20 scans was first taken on a sample of reduced cytochrome c without CW illumination. Then, a cross section was taken from each of the 20 sets of TAS data at the wavelength 430 nm which corresponded to a transient feature in the TAS data. The 20 cross sections were then used to compute a series of 20 averaged cross section beginning at 1 set and ending at 20 sets averaged together. Kinetic fits using Equation A.1 with two terms were then computed on each of the averaged cross sections. Then, the sum of squared residuals (SSR) was computed for each set and corresponding fit (Equation A.2).

$$SSR = \left\|r\right\|_2^2 = \sum_i \left(A_{\lambda,fit}(t_i) - A_{\lambda,data}(t_i)\right)^2 \tag{A.2}$$

The SSRs were then normalized to the highest norm value and plotted as a function of the number of averaged sets. Thresholds were superimposed on the plot (Fig. A.1(c)) to indicate where the norm has reduced to below 20% and 10% of the initial value from 1 scan.

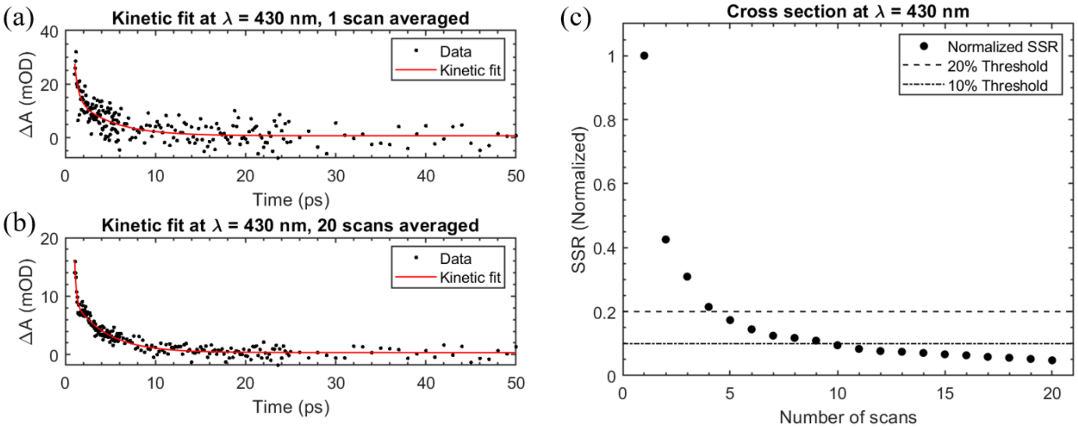

Figure A.1 Transient absorption data (black), along with kinetic fitting curves (red) according to Equation A.1, at 430 nm for cytochrome c with pump wavelength 418 nm are displayed with (a) 1 scan averaged together and (b) 20 scans averaged together. (c) The SSRs of the fit and data are plotted as a function of the number of scans averaged.

Figure A.1 displays an analysis on reduced Cyt c using 20 scans without CW light to determine the number of replicate measurements that are needed for CW-TAS. Figure A.1(a) and A.1(b) are cross sections taken from reduced Cyt c's TAS data at the wavelength 430 nm, corresponding to a transient signal, after (a) 1 scan and (b) 20 averaged scans. For each set of averaged scans from 1-20, a kinetic fit was performed at 430 nm using Equation A.1 with two terms. The SSR was computed using Equation 3 for each number of averaged scans and plotted in Figure A.1(c). Approximately 5 scans were necessary to reduce the SSR, with respect to the data, to 20% while 10 scans were needed to reduce it below 10%.

Examining Figure A.1(c), the SSRs as a function of the number of averaged scans appeared to follow a decaying exponential trend. When performing this analysis at different wavelengths in the TAS data, the number of necessary scans can increase or decrease depending on experimental parameters. The intensity of the probe pulse, as well as the stability of its intensity, affect the signal to noise of the TAS data and hence the number of necessary replicate scans needed. This was necessary to reduce the error in fitting routines, such as kinetic analysis and singular value decomposition, which extract time constants from the TAS data and can have large standard deviations when the noise is significant.

A.2. TAS of reduced cytochrome c using 418 nm pump

Methods used to collect TAS data of Cyt c were the same as described in Chapter 3.2.2 of the main text with a few changes. The pump pulse generated from the 800 nm light source was split using an OPA and converted to 418 nm in this case in order to excite at the Soret band rather than at the Q band. Additionally, the supercontinuum was generated using the sapphire window rather than the CaF_2 window, in order to produce a supercontinuum that covers the visible (VIS) region as shown in Fig. A.2.

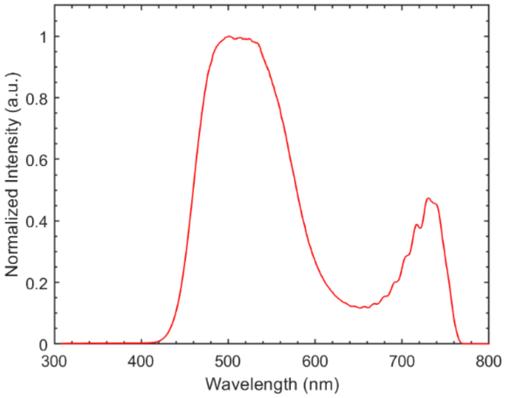

Figure A.2 Supercontinuum spectra generated from the Sapphire window.

Figure A.3 displays the resulting TAS data of Cyt c using the 418-nm excitation wavelength and the VIS supercontinuum. Twenty-one scans were taken and averaged to produce the surface in Fig. A.3(a). Negative transients were observed at 520 and 550 nm corresponding to the absorbance peaks in the Q band of Cyt c's ground state absorption spectra (Fig. 3.3), and therefore appear as ground-state bleaching in TAS. Additionally, the positive transients, with peaks at ~495 and 575 nm, observed on both sides of the Q band bleaching peaks corresponded to excited state absorptions.

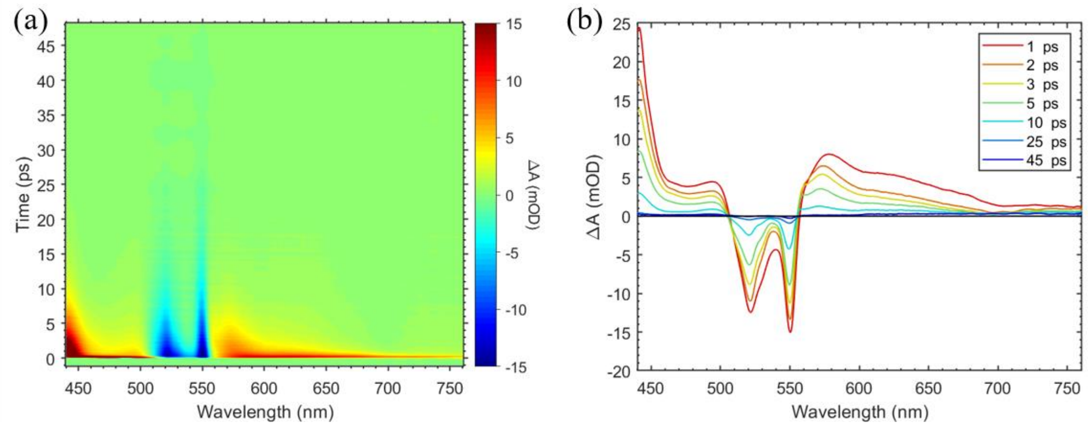

Figure A.3 Transient absorption spectra of Cyt c with 418-nm pump at 200 nJ/pulse displayed as a (a) surface and (b) spectral cross sections at different time delays.